

Mohamed Khider University of Biskra Faculty of exact sciences Scinces of Matter Department

# **Master's Thesis**

Field: Material Sciences Major: Chemistry Specialization: Materials Chemistry Réf.: Entrez la référence du document

> Presented by: **Mayar BENBRAHIM** 03/06/2025

# Electronic, structural and optical properties of barium titanate :DFT calculation

#### Jury: Dr Kamel Djail **MCB** University of Biskra Président Dr Hanane DJOUAMA MCA University of Biskra Supervisor Dr **Imane Seghir MCB** University of Biskra Examiner

AcademicYear: 2024-2025

# Acknowledgements

I would like to express my deepest gratitude to Mrs. **Hanane DJOUAMA**, my research supervisor, for her continuous support, availability, and valuable guidance throughout the course of this work

My sincere thanks also go to Professor Djail Kamel, Supervising Professor, and Assistant Professor Imane Seghir, for their kind supervision.

Many thanks to my friend Dr. oumnia for her support.

This work was carried out jointly within the Laboratory of Applied Chemistry

(LCA) at the University of Mohamed Khider Biskra and the HPC provided by the University of Batna

Please accept my sincere thanks for the great honor you have given me by

accepting to supervise this work

# Personal Acknowledgments

I would like to express my profound gratitude to my beloved **father** and **mother** for their unconditional love, endless patience, and unwavering support throughout every stage of my life. Their sacrifices and encouragement have been the foundation of my academic journey.

A special thank you goes to my dear sisters, Saliha and Fadwa, for always believing in me and standing by my side with love and motivation.

To my **brother Doudou**, thank you for your support, your humor, and your constant encouragement which helped me stay positive during challenging times.

I am also truly grateful to my cherished friends **Douaa** and **Abir** and rania iman ferdous zobida aycha ikram for their kindness, support, and uplifting presence during this period. Your friendship means a great deal to me, and I am thankful to have shared this journey with you.

**Abstract** 

In this work, we report the study of new nanocomposite materials based on barium titanate

BaTiO<sub>3</sub> and polyethylene glycol (PEG). The density functional theory (DFT) computational codes

are used, in practice, to predict the structural, electronic and optical properties of BaTiO<sub>3</sub> and

BaTiO<sub>3</sub>/PEG nanocomposite compounds. Calculated geometric parameters of studied materi-

als are in good agreement with the available experimental values. The theoretical absorption

spectra reproduce the main properties of the experimental spectra. Our results revealed that

the BaTiO<sub>3</sub>/PEG nanocomposite exhibited a high level of molecular stability.

Overall, this study provides a comprehensive theoretical framework for selecting the optimal

functional in DFT-based studies of BaTiO<sub>3</sub>. This lays the groundwork for the rational design and

computational engineering of BaTiO<sub>3</sub>-based materials for next-generation electronic, optical,

and sensing technologies.

**Keywords:** DFT, TD-DFT, BaTiO<sub>3</sub>, polyethylene glycol

Resume

Dans ce travail, nous présentons une étude de nouveaux matériaux nanocomposites à

base de titanate de baryum (BaTiO<sub>3</sub>) et de polyéthylène glycol (PEG). Les calculs basés sur

la théorie de la fonctionnelle de la densité (DFT) sont utilisés, en pratique, pour prédire les

propriétés structurales, électroniques et optiques des composés BaTiO<sub>3</sub> et du nanocomposite

BaTiO<sub>3</sub>/PEG. Les paramètres géométriques calculés des matériaux étudiés sont en bon accord

avec les valeurs expérimentales disponibles. Les spectres d'absorption théoriques reproduisent

les principales caractéristiques des spectres expérimentaux. Nos résultats ont révélé que le

nanocomposite BaTiO<sub>3</sub>/PEG présente un haut niveau de stabilité moléculaire. Dans l'ensemble,

cette étude fournit un cadre théorique complet pour le choix optimal de la fonctionnelle dans

les études basées sur la DFT du BaTiO<sub>3</sub>. Elle jette ainsi les bases pour la conception rationnelle

et l'ingénierie computationnelle de matériaux à base de BaTiO3 destinés aux technologies élec-

troniques, optiques et de détection de prochaine génération.

Mots clés: DFT, TD-DFT, polyéthylène glycol BaTiO<sub>3</sub>

# **Table of contents**

General Introduction				1
1	Literature review			3
	1.1	Introd	luction	4
	1.2	Perovs	skite familly:	5
	1.3	BaTiO	<sub>3</sub> properties	6
		1.3.1	Electronic Properties of BaTiO <sub>3</sub> :	6
		1.3.2	Optical properties of BaTiO <sub>3</sub>	8
		1.3.3	Structural properties BaTiO <sub>3</sub>	9
	1.4	PEG p	properties	10
		1.4.1	Introduction:	10
		1.4.2	Structural Properties of Polyethylene Glycol (PEG)	10
		1.4.3	Electronic Properties of Polyethylene Glycol (PEG)	11
		1.4.4	Optical Properties of Polyethylene Glycol (PEG)	11
2	The	oretica	al And Methodological reminders	13
2.1 Introduction		luction	14	
	2.2	Schrö	odinger Equation	14
	2.3	Found	dations of Density Functional Theory	15
		2.3.1	Key Foundations of DFT	15
		2.3.2	Challenges and Improvements	20
	2.4	Hybri	id Functionals:	21
		2.4.1	The Functional CAM-B3LYP	22

		2.4.2	The PBE functional (Perdew-Burke-Ernzerhof)	22
		2.4.3	M062X Hybrid Meta-Functional: Advancements in Thermochemical and	
			Noncovalent Interaction Descriptions	24
3	Res	ults an	d discussion	25
	3.1	Introd	duction	26
I	Str	uctur	ral electronic and optical studies of Barium Titanate (BaTiO <sub>3</sub> )	27
	3.2	Intro	duction	28
	3.3	Comp	outational method	28
	3.4	Struct	tural electronic and optical studies of Barium Titanate [BaTiO <sub>3</sub> ] <sub>1</sub> :	29
		3.4.1	structural properties:	29
		3.4.2	Electronic properties:	30
		3.4.3	$\label{eq:convergence} \text{UV-Visible Spectroscopy of } [\text{BaTiO}_3]_1 :  \dots  \dots  \dots  \dots  \dots$	31
		3.4.4	IR Vibration Frequencies of $[BaTiO_3]_1$	34
	3.5	Struct	tural electronic and optical studies of Barium Titanate $[BaTiO_3]_c$ :	36
		3.5.1	Structural properties:	36
		3.5.2	Electronic properties:	37
		3.5.3	$UV\text{-}Visible \ Spectroscopy \ of \ [BaTiO_3]_c\text{:} \dots \dots$	38
		3.5.4	IR Vibration Frequencies of $[BaTiO_3]_c$	45
II	St	ructu	ral electronic and optical studies of BaTiO <sub>3</sub> /PEG	48
•••	3.6		duction	49
	3.7		tural electronic and optical studies of polyethylene glycol (PEG):	49
	3.1	3.7.1	Structural properties of PEG:	49
		3.7.2	Electronic properties:	50
		3.7.3	UV-vis spectroscopy	51
		3.7.4	IR Vibration Frequencies:	53
	3.8		tural electronic and optical studies of BaTiO <sub>3</sub> /PEG:	54
	5.0	3.8.1	Modelling of the BaTiO $_3$ /PEG nanocomposite	
		3.0.1	modeling of the parto3/1 bo hanocomposite	55

3.8.2	Structural properties of the BaTiO $_3$ /PEG nanocomposite :	56
3.8.3	Frontier molecular orbitals (FMOs)	57
3.8.4	UV-vis spectroscopy	58
3.8.5	IR Vibration Frequencies:	63
Conclusion générale		
III Annex	1	67
References		73

# **List of Figures**

1.1	Phase transitions of BaTiO <sub>3</sub> as a function of temperature, showing changes in crys-	
	tal structure and relative dielectric constant	4
1.2	Structure of cubic BaTiO $_3$	5
1.3	MUnit cell of metal halide perovskite. Here, A is an organic or inorganic cation, M	
	is a divalent metal cation, and X is a halide anion	6
1.4	UV-Vis absorption spectrum of BaTiO <sub>3</sub> nanoparticles	8
1.5	PL spectrum of BaTiO <sub>3</sub> nanoparticles	9
3.1	Structures of BaTiO <sub>3</sub> and PEG: (a) BaTiO <sub>3</sub> and (b) PEG	26
3.2	Structures of BaTiO <sub>3</sub>	28
3.3	Optimized structures for ([BaTiO $_3$ ] $_1$ ) at the CAM-B3LYP/Lanl2DZ level of theory $\;$	30
3.4	Frontier MO of $[BaTiO_3]_1$ at CAM- $B3LYP/LANL2DZP$ and $B3LYP/LANL2DZP$ level	
		31
3.5	$Molecular\ orbitals\ of\ [BaTiO_3]_1 using\ B3LYP \qquad \dots \qquad \dots \qquad \dots \qquad \dots$	32
3.6	Molecular orbitals of [BaTiO <sub>3</sub> ] <sub>1</sub> using CAM-B3LYP	33
3.7	$Simulated\ uvvis\ spectra\ of\ [BaTiO_3]_1\ at\ CAM-B3LYP/LANL2DZP\ and\ B3LYP/LANL2DZP\ an$	ZP
	level	34
3.8	Simulated IR spectra of CAM-B3LYP for $[BaTiO_3]_1$	35
3.9	Simulated IR spectra of B3LYP for $[BaTiO_3]_1$	35
3.10	Optimized structures for ([BaTiO3]c) at the CAM-B3LYP/Lanl2DZ and B3LYP, M062X	
	level of theory	36
3.11	Frontier MO of $[BaTiO_3]_c$ at CAM- $B3LYP/LANL2DZP$ , $B3LYP/LANL2DZP$ and $M062XP$	/LANL2D2
	level	38

3.12	Molecular orbitals of $[BaTiO_3]_c$ using $B3LYP$ $\hdots$	40
3.13	Molecular orbitals of $[BaTiO_3]_c$ using CAM-B3LYP	42
3.14	Molecular orbitals of $[BaTiO_3]_c$ using M06-2X	43
3.15	Simulated UV–visible spectra of CAM-B3LYP , B3LYP and M062X of BaTiO $_3$	45
3.16	Simulated IR spectra of M062X for $[BaTiO_3]_c$	46
3.17	Simulated IR spectra of CAM-B3LYP for BaTiO $_{3c}$	46
3.18	Simulated IR spectra of B3LYP for $[BaTiO_3]_{\mbox{\scriptsize c}}$	47
3.19	the PEG optimized molecule for CAM/B3LYP	49
3.20	Frontier MO of PEG	51
3.21	Molecular orbitals of PEG using CAM-B3LYP	52
3.22	Simulated UV-visible spectra of PEG	52
3.23	UVvisible spectra of PEG (1):TDDFT and (2):Experimentally	53
3.24	Simulated IR spectra OF PEG	54
3.25	the BaTiO $_3$ /PEG optimized molecule for CAM/B3LYP DFT calculation	56
3.26	The representation of the molecular orbitals of BaTiO <sub>3</sub> /PEG optimized for each	
	Func- tional Hybrid and their HOMO–LUMO's Energy Gap	57
3.27	Molecular orbitals of BaTiO $_3/PEG$ using CAM-B3LYP	60
3.28	Molecular orbitals of BaTiO $_3/PEG$ using CAM-B3LYP	61
3.29	Molecular orbitals of BaTiO $_3/PEG$ using CAM-B3LYP	62
3.30	The UV–visible spectrum of BaTiO <sub>3</sub> /PEG	63
3.31	Simulated IR spectra of BaTiO $_3$ /PEG	64
3.32	Gaussian.	68
3.33	GaussView	69
3.34	OriginPro	69
3.35	Mercury	70
3.36	ChemDraw	71
3.37	Cycle of the study of a molecule by molecular modeling	71

# List of source codes

**CAM-B3LYP** Coulomb-Attenuated B3LYP

**DFT** Density Functional Theory

**HOMO** Highest Occupied Molecular Orbital

**LUMO** Lowest Unoccupied Molecular Orbital

LANL2DZ Los Alamos National Laboratory 2 Double-Zeta

**TDDFT** Time-Dependent Density Functional Theory

**UV–Vis** UltraViolet-Visible

M06-2X meta-hybrid generalized gradient approximation (meta-GGA) functional

**IR** Infrared Spectroscopy

**PEG** Polyethylene Glycol

 $\mathbf{6\text{-}311G(d,p)}$  A triple-zeta split-valence basis set

# **General Introduction**

Barium titanate BaTiO<sub>3</sub> is a multifunctional ceramic material belonging to the class of ferroelectrics, known for its exceptional dielectric constant, ferroelectric behavior, and nonlinear optical properties. These characteristics make it a promising candidate for a wide range of technological applications, including high-performance capacitors, transducers, actuators, sensors, and photovoltaic devices. Furthermore, the ability to tailor its electronic and structural behaviors through nanocomposites opens a path toward the design of custom materials for specific optoelectronic applications.[22]

In this work, we investigate the structural, electronic and optical properties of  $BaTiO_3$  using DFT-based simulations with a comparative evaluation of three different hybrid functionals. The goal is to determine which functional offers the most accurate description of the material, particularly in the context of future nanocomposites strategies.

### **Objective**

The principal aim is to predict the precise structural model of the newly developed  $BaTiO_3/PEG$  hybrid material and expansively analyze its properties, including structural, optoelectronic. This comprehensive investigation not only provides valuable insights into the nanocomposite's geometric characteristics, such as bond lengths and dihedral angles between atoms, but also enhances our understanding of its fundamental Optical properties and applications.

In this context, the thesis is organized as follows:

- Chapiter 1: Literature review The objective of this chapter is to provide a comprehensive overview of the existing research related to the structural, electronic, and optical properties of barium titanate (BaTiO<sub>3</sub>). It aims to establish a solid theoretical foundation by summarizing key findings and methodologies from previous studies. Additionally, this chapter highlights the role of polyethylene glycol (PEG)
- Chapiter 2: Theoretical And Methodological reminders The objective of this chapter is to present the theoretical and methodological foundations relevant to the present work. It provides a general overview of Density Functional Theory (DFT), including its fundamental principles, approximations, and its role in the calculation of structural, electronic, and optical properties of materials. This chapter aims to equip the reader with the essential theoretical background and computational methods used in the study.
- **Chapitr 3: Conception** The objective of this chapter is to present and analyze the results of the structural, electronic, and optical properties of BaTiO<sub>3</sub> and PEG using Density Functional Theory (DFT) calculations. The study includes the individual analysis of both materials and explores the effects of doping BaTiO<sub>3</sub> with PEG. All simulations were performed using Gaussian software and GaussView interface, aiming to understand the impact of PEG incorporation on the physical properties of BaTiO<sub>3</sub>.

Finally, we will conclude our work with a general conclusion.

# Chapter 1

# Literature review

### 1.1 Introduction

Barium titanate BaTiO<sub>3</sub> has been a material of significant interest for over 60 years due to its high mechanical and chemical stability, ferroelectric properties at and above room temperature, and ease of preparation as polycrystalline ceramic samples. As a versatile perovskite, BaTiO<sub>3</sub> finds applications in optical modulators, electromechanical transducers, and infrared sensors due to its high dielectric constant and remarkable pyroelectric, piezoelectric, and electro-optic effects. [43] [19]

BaTiO<sub>3</sub>-based ceramics are widely used in capacitors and show promising potential for electrooptical applications due to their stable performance at room temperature. Below 120 °C,  $Ti^{4+}$  ions shift towards a vertex of the oxygen octahedron in the crystal lattice, inducing a transition from a cubic to a tetragonal structure. This tetragonal phase remains stable between 5°C and 120°C, but further cooling leads to an orthorhombic phase transition. [44]

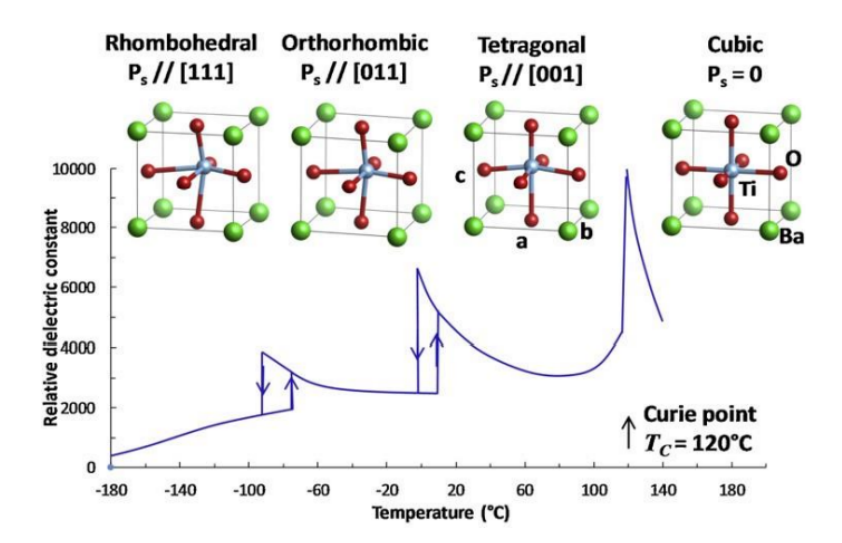


Figure 1.1: Phase transitions of BaTiO<sub>3</sub> as a function of temperature, showing changes in crystal structure and relative dielectric constant.

[13]

To overcome practical limitations, chemical doping is often employed to enhance the properties of BaTiO<sub>3</sub>. Doping modifies the Curie temperature ( $T_c$ ) through ion-size effects and changes

in the tolerance factor while also improving conductivity via donor electron compensation. Rare-earth elements, which are known for their strong electronic charges and large ionic radii, are particularly effective dopants that enhance both the mechanical and electrical properties of BaTiO<sub>3</sub> ceramics. [42]

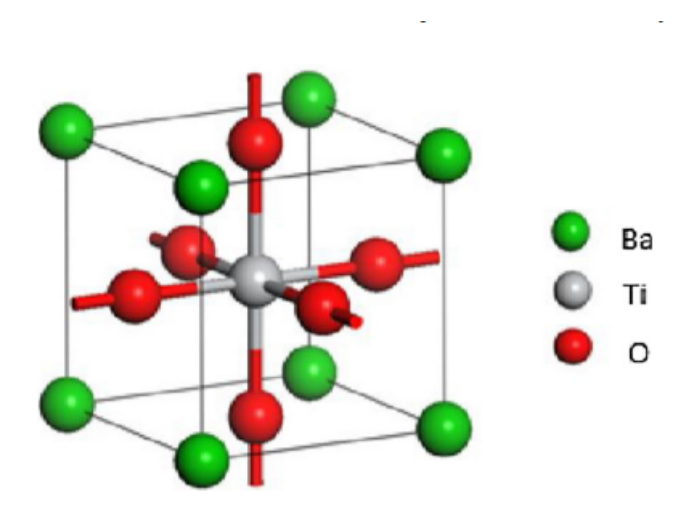


Figure 1.2: Structure of cubic BaTiO<sub>3</sub>

One of the most interesting applications of BaTiO<sub>3</sub> is its role as a semiconductor with a positive temperature coefficient of resistivity (PTCR). Achieving enhanced PTCR properties requires the addition of dopants to the host titanate. Trivalent rare-earth elements can be substituted into the perovskite lattice, inducing semiconducting behavior. Similarly, pentavalent dopants, such as Sb, Nb, and Ta, can also introduce semiconduction by substituting at  $Ti^{4+}$  lattice sites. [10]

### 1.2 Perovskite familly:

Today the term 'perovskite' is used to designate the crystalline structure of a wide variety of ABX<sub>3</sub> ionic compounds with similar type of ionic. However, historically this name was used for a specific material, which has been coined for the mineral calcium titanate (CaTiO<sub>3</sub>) (**Figure 1.3**). crystalline structure. Depending on the ion radii, the ideal cubic structure may deform into structures with a lower symmetry. The perovskite structure can accommodate different dopant

cations providing opportunities to change the material properties.

This mineral has been discovered in the Ural Mountains of Russia. The first sample of the mineral was transferred from Saint Petersburg to Berlin in 1839 by the Russian mineralogist Alexander Kämmerer, who gave the sample for further investigation of the German mineralogist and crystallographer Gustav Rose. Rose determined its properties and chemical composition and named the mineral after Russian politician and mineralogist Lev Perovskite.[27]

In particular, BaTiO<sub>3</sub>, an extensively studied perovskite material, is known for its **ferroelectric behavior and high dielectric constant**, making it indispensable in electronic and energy storage applications. The ability to tailor perovskite compositions through dopants and structural modifications has further expanded their relevance in modern material science and nanotechnology, including in **biomedical and environmental applications**.[39]

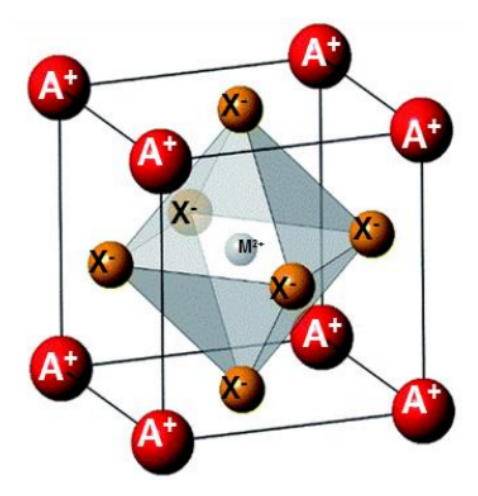


Figure 1.3: MUnit cell of metal halide perovskite. Here, A is an organic or inorganic cation, M is a divalent metal cation, and X is a halide anion.

### 1.3 BaTiO<sub>3</sub> properties

#### **1.3.1** Electronic Properties of BaTiO<sub>3</sub>:

#### • Band Gap Characteristics:

The electronic bandgap of BaTiO<sub>3</sub> is strongly influenced by its structural phase transitions

and temperature variations. First-principles calculations and experimental studies confirm that BaTiO<sub>3</sub> exhibits an indirect band gap, with values of approximately 3.15 eV in the tetragonal phase (C-A transition) and 3.12 eV in the cubic phase (C-R transition). Quasiparticle self-energy corrections from GW calculations significantly increase these values to 3.68 eV (cubic) and 3.90 eV (tetragonal), aligning more closely with experimental optical gap measurements (3.3 eV). The band gap decreases systematically with increasing temperature, exhibiting a sharp anomaly at 393 K, corresponding to the tetragonal-to-cubic phase transition. This transition is accompanied by electronic heterogeneity and disorder, as indicated by variations in Urbach energy (Eu) and Urbach focus (E<sub>0</sub>), confirming phase coexistence . Furthermore, excitonic effects play a crucial role, with an exciton binding energy of nearly 1 eV, explaining the deviation between the optical absorption onset and the GW-calculated band gap. The conduction band minimum (CBM) is primarily dominated by Ti 3d orbitals, while the valence band maximum (VBM) is composed mostly of O 2p states, with minor contributions from Ba states . The findings emphasize the critical impact of structural phase transitions and temperature on the electronic and optical properties of BaTiO<sub>3</sub>, making it a key material for ferroelectric and optoelectronic applications.[45] [36]

However, doping can significantly alter the electronic band structure and modify the bandgap characteristics.

A notable example is lanthanum (La) doping, in which La atoms substitute barium (Ba) sites in the crystal lattice. This substitution introduces additional electronic states, which shift the CBM and VBM, leading to a transition from an indirect to a direct bandgap. In a direct band gap, both the CBM and VBM are located at the same k-point, allowing electrons to transition without phonon interactions, thereby enhancing the optical absorption and electrical conductivity. Additionally, La doping reduces the band gap energy, facilitating easier electronic transitions and making the material more suitable for optoelectronic applications such as sensors and electro-optic devices.[42]

Experimentally, the band gap of pure BaTiO<sub>3</sub> is reported to be approximately 3.19 eV, corresponding to the optical band gap measured through UV-Vis spectroscopy. However, density functional theory (DFT) calculations tend to underestimate this value, typically predicting a

smaller bandgap. This discrepancy arises due to the limitations of standard generalized gradient approximation (GGA) and local density approximation (LDA) functionals, which do not fully account for electron exchange-correlation interactions. [51][15]

#### **1.3.2** Optical properties of BaTiO<sub>3</sub>

Optical characterization of  $BaTiO_3$  nanoparticles synthesized via the electrochemical route revealed distinct absorption and emission behaviors, and Fourier transform infrared (FTIR) spectroscopy identified key vibrational modes associated with Ti-O, Ti-OH, and Ba-OH bonds, highlighting the chemical interactions within the material. UV-Vis absorption spectra demonstrate a peak at 330 nm, corresponding to an estimated band gap energy of 3.1 eV, which aligns with the typical values for  $BaTiO_3$ , indicating its strong potential for optoelectronic applications. [7]

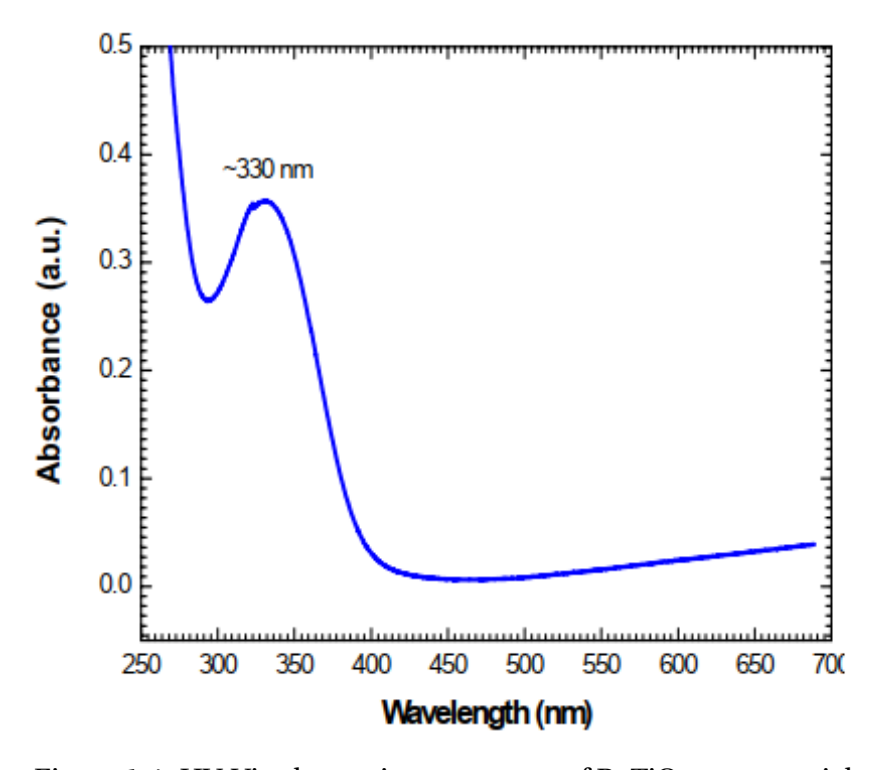


Figure 1.4: UV-Vis absorption spectrum of BaTiO<sub>3</sub> nanoparticles.

• A photoluminescence (PL) spectrometer is used to measure electronic excitement, electron configurations, defects, impurities, and the rate recombinations in semiconducting nanomaterials.[47] and the photoluminescence (PL) spectrum of BaTiO<sub>3</sub> nanoparticles exhibits defect-related deep-level emissions in the visible range. This emission is

attributed to the recombination of electrons and holes within delocalized states, which arises from the intrinsic structural defects associated with symmetric  $Ti^{3+}$  sites in the nanophase barium titanate. The PL response was closely linked to the exponential optical absorption edge and tail states. The observed PL behavior stems from radiative recombination between the trapped electrons and holes in these tail states. A broad emission band is distinctly centered around  $\sim 545$  nm ( $\sim 2.275$  eV), accompanied by a shoulder peak at  $\sim 557$  nm ( $\sim 2.226$  eV), which is characteristic of the oxygen vacancy-induced emission. In this study, oxygen vacancies within  $BaTiO_3$  nanoparticles acted as primary emission sources under photoexcitation and played a significant role in determining the PL properties.[7]

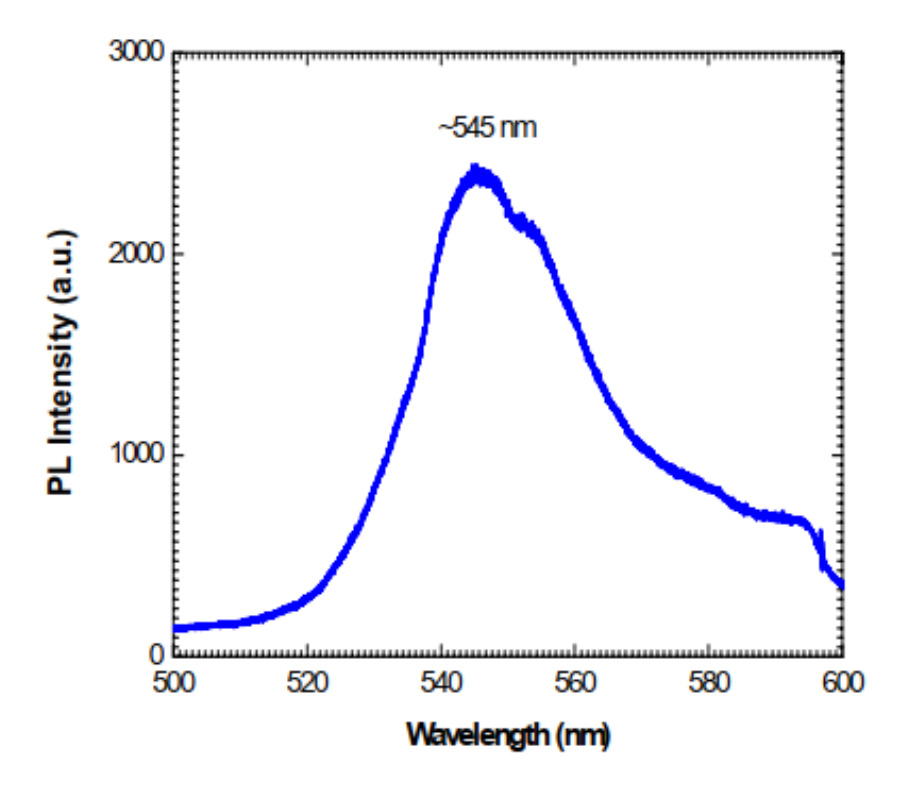


Figure 1.5: PL spectrum of BaTiO<sub>3</sub> nanoparticles.

### **1.3.3** Structural properties BaTiO<sub>3</sub>

BaTiO<sub>3</sub> exhibits cubic symmetry in its paraelectric phase with a space group of Pm3m. The crystal structure consists of corner-sharing oxygen octahedra interpenetrated by simple cubic

lattices of Ba and Ti cations. The Ti cations are centrally positioned within the oxygen octahedra, whereas Ba ions occupy 12-fold coordinated sites between the octahedral units.

To optimize the structural parameters of BaTiO<sub>3</sub>, researchers have performed geometry optimization calculations using the LDA+U method ( $U=4\,\mathrm{eV}$ ). Computational analyses using the CASTEP code confirmed the accuracy of lattice parameter estimations and atomic positions, demonstrating consistency with previous experimental studies. These findings validate the reliability of structural calculations, which are crucial for assessing the material stability and further theoretical investigations of perovskite oxides.

The optimized structural parameters obtained from the LDA+U calculations included a lattice parameter (a) of 3.954 Å and a unit cell volume (V) of 61.80 Å<sup>3</sup>. These values exhibit strong agreement with the experimental measurements, where a is reported as 4.012 Å and V is 63.57 Å<sup>3</sup>. In addition, the atomic bonding distances were determined to be Ba–O at 2.796 Å and Ti–O at 1.977 Å. The unit cell structure of BaTiO<sub>3</sub> consists of Ba atoms (green spheres) positioned at the corners, a Ti atom (silver sphere) at the center, and O atoms (red spheres) located at the center of each cubic face, reinforcing the classical perovskite configuration. [49]

# 1.4 PEG properties

#### 1.4.1 Introduction:

PEG earns its fame because of its high structure flexibility, biocompatibility, amphiphilicity, devoid of any steric hindrances, and high hydration capacity [21]

### 1.4.2 Structural Properties of Polyethylene Glycol (PEG)

Polyethylene Glycol (PEG) is a linear polyether composed of repeating ethylene oxide ( $\text{CH}_2\text{-CH}_2\text{-O-}$ ) units, with terminal hydroxyl functional groups. Its high water solubility, biocompatibility, and hydrophilic nature render it a valuable polymer for biomedical applications. PEG is neutral, non-ionic, and biodegradable, allowing it to be integrated seamlessly into drug delivery systems, tissue engineering, and regenerative medicine. In composite materials such

as hydroxyapatite (HAP)/PEG blends, PEG serves as a structural modifier, enhancing the mechanical properties, biocompatibility, and nanoparticle aggregation. The interaction between PEG and biopolymers facilitates molecular binding through Van der Waals forces and hydrogen bonding, reinforcing its ability to improve stability and dispersion in hybrid materials . [8]

#### 1.4.3 Electronic Properties of Polyethylene Glycol (PEG)

DFT calculations provided insights into the electronic behavior of PEG-based composites. The energy band gap of HAP/PEG was calculated to be 4.61 eV, classifying it as a wide-band gap semiconductor with potential optoelectronic applications. The global hardness (2.30 eV) of the HAP/PEG composite was significantly higher than that of pure HAP (0.65 eV), indicating a greater resistance to chemical reactivity and structural deformation. Moreover, the HOMO-LUMO energy separation (EHOMO/ELUMO = 10.62 eV) suggested high molecular stability, further reinforcing its suitability for chemically stable applications. The maximum charge transfer index ( $\Delta$ Max = 1.20 eV) indicates substantial intermolecular charge transfer ability, allowing efficient electron exchange and interaction within the polymer matrix.[8]

### 1.4.4 Optical Properties of Polyethylene Glycol (PEG)

PEG plays a crucial role in modifying the optical transparency and refractive index of the polymeric systems. [1]

#### **Absorbance**

The absorbance of PEG films is strongly influenced by molecular weight, with a higher Mw leading to increased absorption, particularly in the ultraviolet (UV) region (300 nm). The integration of GONSs further amplifies the absorbance, with reported enhancements of up to 71% owing to Mw variations and up to 100% with the addition of GONSs. This increase is attributed to electronic transitions, where electrons in higher energy states absorb electromagnetic radiation and move to elevated energy levels

#### **Transmittance**

The optical transmittance of PEG and its nanocomposites decreased at lower wavelengths (in the UV region). The optimal transmittance for PEG was approximately 98.5%, whereas the PEG-GO composites exhibited slightly reduced transmittance of 96% at longer wavelengths. Increasing Mw and introducing GONSs as nanofillers typically result in a decline in optical transmittance, reinforcing their potential for UV-shielding applications.

#### **Optical Energy Gap**

The optical energy gap of the PEG films, including both allowed and forbidden indirect transitions, decreased with increasing Mw and GONS incorporation. This reduction is primarily linked to structural disorder within the polymer matrix and the tunability of the GO band gap, which influences the material's light absorption properties.[1]

# **Chapter 2**

**Theoretical And Methodological reminders** 

#### 2.1 Introduction

This chapter provides a concise introduction to theoretical computational methods, with a particular focus on Density Functional Theory (DFT), which is widely recognized as a powerful approach for investigating the electronic and structural properties of materials.

DFT has proven to be highly effective for studying the electronic structure and optical properties of complex systems, including perovskite materials such as  $BaTiO_3$ . Given its accuracy and computational efficiency, DFT is an ideal tool for analyzing the fundamental interactions governing the behavior of  $BaTiO_3$  at the atomic and electronic levels. [38]

# 2.2 Schrödinger Equation

The Schrödinger equation is the foundation for almost all computational chemistry methods. It was inductively proposed by Schrödinger in 1926 and describes the motion of electrons and nuclei in molecular systems. The time-independent stationary form of the equation is written as: [46]

$$\hat{H}\Psi = E\Psi \tag{2.1}$$

where  $\hat{H}$  is the total energy operator, called the "molecular Hamiltonian," We obtain the total energy E and the wave function  $\psi$ , from which all information about the studied system can be determined.

The total Hamiltonian  $\hat{H}$  for a system of N nuclei and n electrons, expressed in atomic units, includes the following terms. [5]

$$\hat{H} = \hat{T}_e + \hat{T}_n + \hat{V}_{ee} + \hat{V}_{nn} + \hat{V}_{ne} \tag{2.2}$$

The Schrödinger equation can be solved exactly for simple single-electron systems, such as hydrogen. However, for more complex systems, it is necessary to use approximations, either

on the Hamiltonian or on the form of the wave function itself.[32]

With the nuclei represented by A and B and the electrons represented by k and l, the precise Hamiltonian of a system composed of N nuclei and n electrons is expressed as follows:

$$\hat{H} = -\frac{1}{2} \sum_{k=1}^{n_e} \frac{\hbar^2}{m_e} \nabla_k^2 - \sum_{k=1}^{n_e} \sum_{A=1}^{N} \frac{e^2}{4\pi\varepsilon_0} \frac{Z_A}{r_{kA}} + \sum_{k=1}^{n_e} \sum_{\substack{l=1\\l \neq k}}^{n_e} \frac{e^2}{4\pi\varepsilon_0} \frac{1}{r_{kl}} - \frac{1}{2} \sum_{A=1}^{N} \frac{\hbar^2}{M_A} \nabla_{R_A}^2 + \sum_{A=1}^{N} \sum_{\substack{B=1\\B \neq A}}^{N} \frac{e^2}{4\pi\varepsilon_0} \frac{Z_A Z_B}{R_{AB}}$$
 (2.3)

# 2.3 Foundations of Density Functional Theory

Density Functional Theory (DFT) is a quantum mechanical method used to investigate the electronic structure of many-body systems, particularly atoms, molecules, and solids. This is based on the principle that the ground-state properties of a system can be determined by its electron density rather than its wave function.

The foundation of the density functional theory is that Thomas and Fermi developed soon after quantum mechanics [50] [16] was developed. In the Thomas–Fermi theory of atoms, the energy of a system is expressed as a function of one-particle density, which can be understood as a semiclassical approximation. Over the course of several decades, several writers have expanded this theory by adding further density-dependent variables that were acquired by gradient expansions of the energy Despite being tenable from a practical standpoint, these ideas lacked a solid basis because they attempted to represent the entire energy of a many-particle system as simply a function of the one-particle density. [28]

#### 2.3.1 Key Foundations of DFT

#### **Hohenberg-Kohn Theorems:**

Lies at the heart of DFT ,These theorems establish that the ground-state energy of a many-body system is a unique functional of the electron density. However, the original formulation has faced challenges, leading to further research and refinement to address its limitations [28]

Consider a system of N electrons enclosed in a large box that move under the influence

of a time-independent local external potential v(r). In this section only nondegenerate ground states are considered. The first Hohenberg—Kohn theorem states that v(r) is determined within a trivial additive constant based on the knowledge of the electron density v(r). The proof proceeds through the reductio ad absurdum. Suppose that there exists another potential v'(r) leading to the same densities v(r) and  $v \neq v' + const$ . That means that we have two different ground-state wave functions v(r) and v'(r) and v'(r) and consequently two different Hamiltonians v(r) and v'(r) and

$$\hat{H} = \hat{T} + \hat{V}_{ee} + \sum_{i=1}^{N} \nu(\mathbf{r}_i),$$
 (2.4)

where  $\hat{T}$  and  $\hat{V}_{ee}$  are the kinetic and electron–electron repulsion operators, respectively.

$$\hat{T} = -\frac{1}{2} \sum_{i=1}^{N} \nabla_i^2, \tag{2.5}$$

$$\hat{V}_{ee} = \sum_{i < j}^{N} \frac{1}{r_{ij}},\tag{2.6}$$

$$\hat{V} = \sum_{i=1}^{N} \nu(r_i). \tag{2.7}$$

Atomic units are widely used.

From the Rayleigh–Ritz variational principle it follows that [37]

$$E_0 = \langle \Psi | H | \Psi \rangle < \langle \Psi' | H | \Psi' \rangle = \langle \Psi' | H' | \Psi' \rangle + \langle \Psi' | H - H' | \Psi' \rangle \tag{2.8}$$

$$= E_0' + \int n(r)[v(r) - v'(r)] dr.$$
 (2.9)

Similarly, using the variational principle for the Hamiltonian H' with the trial function  $\Psi$ , we

have [37]

$$E_0' = \langle \Psi' | H' | \Psi' \rangle < \langle \Psi | H' | \Psi \rangle = \langle \Psi | H | \Psi \rangle + \langle \Psi | H' - H | \Psi \rangle \tag{2.10}$$

$$= E_0 + \int n(r) [v'(r) - v(r)] dr.$$
 (2.11)

Addition of Eqs (7) and (8) leads to contradiction and one concludes that the density determines the external potential, consequently the Hamiltonian and thus all electronic properties of the system. If we write the total energy as [37]

$$E_{v}[n] = \int n(r)v(r) dr + F_{HK}[n], \qquad (2.12)$$

The functional  $F_{HK}[n]$  is the sum of the kinetic and electron–electron repulsion energies. The second Hohenberg–Kohn theorem states that for any trial density  $\tilde{n}$ 

$$E_0 \le E[\tilde{n}] \tag{2.13}$$

if  $\tilde{n}(r) \ge 0$  and  $N = \int \tilde{n}(r) dr$ . The proof is based on the variational principle as for any trial wave function  $\tilde{\Psi}$ 

$$\langle \tilde{\Psi} | \hat{H} | \tilde{\Psi} \rangle = \int \tilde{n}(r) v(r) dr + F[\tilde{n}] = E_{\nu}[\tilde{n}] \ge E_{\nu}[n]. \tag{2.14}$$

Equality stands only in the true ground state.

The variation of the total energy at constant number of electrons [37]

$$\delta \left\{ E_{\nu}[n] - \mu \left[ \int n(r) dr - N \right] \right\} = 0 \tag{2.15}$$

leads to the Euler equation [37]

$$\mu = \frac{\delta E_{\nu}[n]}{\delta n} = \nu(r) + \frac{\delta F_{\text{HK}}[n]}{\delta n}.$$
 (2.16)

The functional  $F_{HK}[n]$  is defined exclusively for trial densities n(r) that are v-representable. A density is considered v-representable if it corresponds to the ground-state wave function of the Hamiltonian under the influence of a local external potential. However, the precise conditions necessary for a density to be v-representable remain undetermined. Previous studies have demonstrated the existence of a universal variational functional that accurately accounts for the total kinetic and electron-electron repulsion energies without requiring the density to be v-representable. [37] [28]

#### **Kohn-Sham Equations:**

These auxiliary equations are used to simplify the problem by introducing non-interacting particles that have the same density as the interacting system. The challenge lies in accurately approximating the exchange-correlation potential, which accounts for many-body interactions [37] [28] According to the Kohn-Sham formalism, the electronic energy of the ground state of a system consisting of n electrons and N nuclei can be described as follows (in atomic units, a.u.):

$$E[\rho] = -\frac{1}{2} \sum_{i=1}^{n} \int \phi_{i}^{*}(r_{1}) \nabla_{i}^{2} \phi_{i}(r_{1}) dr_{1} - \sum_{x=1}^{N} \int \frac{Z_{x}}{r_{xi}} \rho(r_{1}) dr_{1} + \frac{1}{2} \int \int \frac{\rho(r_{1})\rho(r_{2})}{r_{12}} dr_{1} dr_{2} + E^{xc}[\rho],$$
(2.17)

The electronic density  $\rho(r)$  of the system is

$$P(r) = \sum_{i=1}^{n} n_i |\phi_i(r)|^2$$
 (2.18)

First, they assumed the existence of a fictitious system of N independent electrons with a density in its ground state  $\rho_{\rm fond}(r)$ . The significance of this assumption lies in the fact that the expressions for the kinetic and potential energies of this fictitious system are known. Then, they showed that, for this to be the case, these electrons must be immersed in an effective external potential. This is the first Kohn-Sham (K.S.) equation given by  $V_{\rm eff}[\rho(r)]$ .

$$V_{\text{eff}}[\rho(\vec{r})] = V_H(\vec{r}) + V_{\text{xc}}[\rho(\vec{r})] + V_{\text{ext}}(\vec{r})$$
 (2.19)

•  $V_{\text{ext}}(\vec{r})$ : The external potential

•  $V_H(\vec{r})$ : The Hartree potential

•  $V_{\rm xc}[\rho(\vec{r})]$ : The exchange-correlation potential

$$[\rho(\vec{r})] = \frac{\delta E_{xc}[\rho]}{\delta \rho(\vec{r})} \tag{2.20}$$

 $E_{xc}$  is the exchange-correlation energy, which includes the correlation effects caused by the quantum nature of electrons as well as anything else that is not known directly about the system.

It is easy to obtain  $V_{xc}$  when  $E_{xc}$  is known. Kohn-Sham orbitals are significant because they make it possible to compute the density using equation (2.15). Starting from an initial density, which for a molecular system can simply be the superposition of the electronic densities of the atoms, the Kohn-Sham equation solution is handled in a self-consistent manner.

The initial Kohn-Sham orbitals were obtained by solving the Kohn-Sham equations using this process. The improved density was then calculated from equation (2.15)using the initial set of orbitals. This procedure was repeated until the exchange-correlation energy and electronic density met a carefully selected convergence threshold. Equation (2.14) was then used to obtain the electronic energy of the system.

#### **Exchange-Correlation Functionals:**

The accuracy of the DFT depends heavily on the approximations used for these functionals. Despite their approximations, they often yield reasonable results for molecular and condensed matter properties [37] [28]

The exchange-correlation energy  $E_{XC}$  is generally divided into two separate terms: the exchange term  $E_X$  and the correlation term  $E_C$ . The exchange term is typically associated with the interactions between electrons with the same spin, whereas the correlation term mainly represents the interactions between electrons with opposite spins.

$$E_{xc}[\rho] = E_x[\rho] + E_c[\rho] \tag{2.21}$$

The second Kohn-Sham (K.S.) equation uses this effective potential in the N single-electron Schrödinger equations to obtain( $\varphi_i$ ).

$$V_{\text{eff}}(\mathbf{r}) \rightarrow \left(-\frac{1}{2}\nabla^2 + V_{\text{eff}}(\mathbf{r})\right)\phi_i(\mathbf{r}) = \varepsilon_i\phi_i(\mathbf{r})$$
 (2.22)

The density can be derived from N single-electron wave functions by using the third equation:

$$\phi_i(\mathbf{r}) \to \rho(\mathbf{r}) = \sum_{i=1}^N |\phi_i(\mathbf{r})|^2$$
 (2.23)

DFT maintains its accurate formalism when used in conjunction with the Kohn-Sham orbital method. A universal functional  $F_{HK}[\rho]$  and, ultimately, the exchange-correlation energy  $E_{xc}[\rho]$  gradually replace the unknown portion of the functional  $E[\rho]$ . The expression of this exchange-correlation functional, which depends on a specific number of approximations, must now be approximated.[5]

#### 2.3.2 Challenges and Improvements

#### **N-Representability Conditions:**

Recent advancements have focused on the application of N-representability conditions to improve the accuracy of DFT functionals. These conditions ensure that the reduced density matrices used in calculations are physically meaningful [28]

#### **Local-Scaling Transformation DFT (LS-DFT):**

This approach addresses some foundational issues in traditional DFT by incorporating N-representability conditions from the outset, although its practical application to large systems remains limited due to technical challenges [28]

#### **Time-Dependent DFT (TDDFT):**

An extension of DFT to time-dependent systems, TD-DFT, was used to study the electronic spectra and dynamics. It reformulates time-dependent quantum mechanics using electron

density as the fundamental variable [34] [35]

## 2.4 Hybrid Functionals:

It is also important to discuss "hybrid" functionals, which belong to a different family of exchange and correlation functionals. In contrast to the Local Density Approximation (LDA), these functionals retain the correlation component while incorporating all or a portion of the Hartree-Fock exchange within the Kohn-Sham formalism. Results similar to those of the Generalized Gradient Approximation (GGA) approach were obtained when the HF exchange component was used in conjunction with GGA functionals. The "half-and-half" functional, which incorporates 50% Hartree-Fock exchange was the first functional of this kind to be presented by Becke.

Using the Lee, Yang, and Parr (LYP) approximation, Becke introduced a functional in the form of a three-parameter expression B3. The codes used for these functionals were B3LYP, B3P86, and B3PW91.[31] The B3LYP functional is currently one of the most popular among them. It produces outstanding results, especially when studying transition-metal organometal-lic compounds.

It consists of three parameters: a Hartree-Fock exchange term, correction to this term (LDA), and correlation term (GGA)[23]. The idea is to adjust the percentage of HF exchange and DFT exchange based on the inter-electronic distance, as exchange effects become dominant at long distances. In long-range corrected (LC) hybrid functionals, the exchange term is split into two components: short-range and long-range. Each of these terms has a different percentage of Hartree-Fock exchange. An example of such an LC functional is the CAM-B3LYP functional. [17]

Finally, studies are being conducted to develop novel hybrid functionals. One prominent example is the Perdew, Burke, and Ernzerhof (PBE0) functional [12], which has shown excellent efficiency for electronic excitation energy estimates, vibrational frequency predictions, and geometry calculations.

#### 2.4.1 The Functional CAM-B3LYP

A novel hybrid exchange–correlation functional, designated as CAM-B3LYP, was introduced. This functional integrates the hybrid characteristics of B3LYP with a long-range correction, as described by Tawada et al. [J. Chem. Phys., in press]. It was demonstrated that CAM-B3LYP produces atomization energies comparable in quality to those obtained using B3LYP, while also exhibiting superior performance for charge transfer excitations in a dipeptide model, which B3LYP significantly underestimates. The CAM-B3LYP functional consists of 0.19 Hartree–Fock (HF) and 0.81 Becke 1988 (B88) exchange interaction at short-range, and 0.65 HF and 0.35 B88 at long-range. the intermediate region was smoothly characterized using the standard error function with a parameter of 0.33, which constitutes a correction to B3LYP and is defined by the following expression:[57]

$$E_X^{B3} = (1 - \alpha)E_X^{Slater} + \alpha E_X^{HF} + C^{B88} \Delta E_X^{B88}$$
 (2.24)

With

- $\alpha = 0.2$ .
- $C^{B88}$  It is a semi-empirical parameter.
- $\Delta E_X^{B88}$  The correction gradient for Becke exchange 1988

#### **2.4.2** The PBE functional (Perdew-Burke-Ernzerhof)

The Perdew-Burke-Ernzerhof (PBE) functional is widely used in density functional theory (DFT), owing to its balance between accuracy and computational efficiency. However, it exhibits systematic errors in predicting the atomization energies, with deviations larger than those observed in the empirical functionals. Despite this, PBE provides comparable accuracy in terms of ionization potential, electron affinity, and bond length. Although it performs well for molecular properties, its modified variant, APBE [12],[14] demonstrates superior accuracy. Additionally, PBE has been found to introduce significant errors in thermochemical predictions, such as heat of formation, necessitating the use of hybrid methods such as PBE0, which incorporates

Hartree-Fock exchange for improved precision.[55]

In the context of adsorption energetics, revised functionals such as revPBE and RPBE have been developed to enhance the accuracy of chemisorption calculations on metal surfaces, addressing some of the inherent limitations of the original PBE formulation. [18]

$$E_{XC}^{PBE} = \frac{1}{4}E_X^{HF} + \frac{3}{4}E_X^{PBE} + E_C^{PBE}$$
 (2.25)

The PBE correction energy is given by

$$E_C^{PBE} = \int \rho(r) \left[ \varepsilon_C^{unif}(r_s, \xi) + H(r, \xi, t) \right] dr$$
 (2.26)

- $\varepsilon_c^{unif}(r_s,\xi)$  It is the correlation energy density of the uniform electron gas.
- $H(r, \xi, t)$  It is the function that accounts for the contribution of the gradient of the correlation energy.

$$r_{s} = \sqrt[3]{\frac{3}{4}\pi\rho(r)}$$
 (2.27)

$$\xi = \frac{\alpha(r) - \beta(r)}{\rho(r)} \tag{2.28}$$

$$t = \frac{|\nabla \rho(r)|}{2\phi k, \rho(r)} \tag{2.29}$$

$$\phi(\xi) = \frac{\left[ (1+\xi)^{2/3} + (1-\xi)^{2/3} \right]}{2} \tag{2.30}$$

$$k_s = \sqrt{\frac{4k_F}{\pi}} \tag{2.31}$$

 $\alpha$  et  $\beta$  They are the spin-up and spin-down density numbers. [12]

# 2.4.3 M062X Hybrid Meta-Functional: Advancements in Thermochemical and Noncovalent Interaction Descriptions

The development of scale factors for modern Minnesota hybrid meta-exchange-correlation functionals, including M05, M05-2X, M06, and M06-2X, plays a crucial role in enhancing the accuracy of computational chemistry methods. These functionals are designed for thermochemistry, thermochemical kinetics, and noncovalent interactions, providing improved performance across various chemical systems The M06-2X functional is distinguished by its incorporation of double nonlocal exchange, specifically optimized for nonmetallic systems. Because of this enhanced parameterization, both M05-2X and M06-2X are well suited for studying nontransition metal-containing molecules. Notably, these functionals have demonstrated their effectiveness in investigating the nucleobase stacking interactions and noncovalent forces within biomolecular structures. Given their versatile applications, the M05, M05-2X M06, and M06-2X functionals are considered essential hybrid meta-functionals for advancing scale factor methodologies [30]

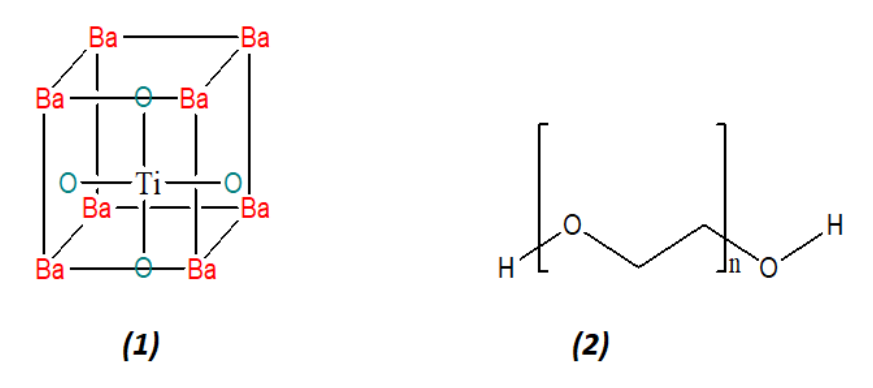
# **Chapter 3**

# **Results and discussion**

## 3.1 Introduction

In this chapter, we present and analyze the computational findings for the structural, electronic, and optical properties of barium titanate BaTiO<sub>3</sub> and BaTiO<sub>3</sub>/PEG nanocomposite obtained from density functional theory (DFT) calculations.

First, we optimized the geometries of both  $[BaTiO_3]_1$  fragment and  $[BaTiO_3]_c$  (cubic) in their ground (S0). Then,  $BaTiO_3/PEG$  nanocomposite has been built starting from the ground-state optimized geometries of  $BaTiO_3$  and PEG structures. (**Scheme3.1**)



Scheme 3.1: Structures of BaTiO<sub>3</sub> and PEG: (a) BaTiO<sub>3</sub> and (b) PEG

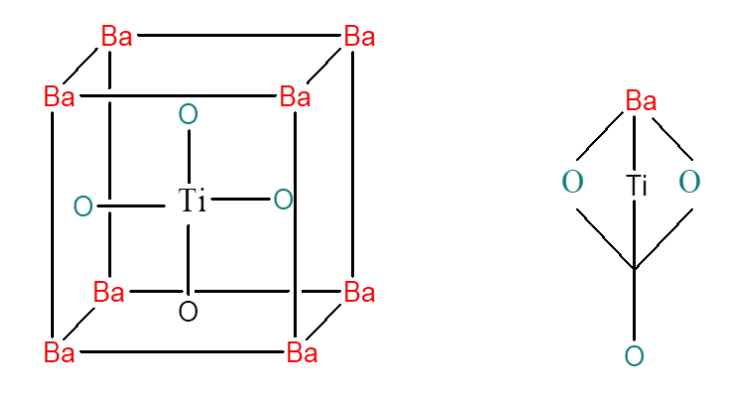
### Part I

# Structural electronic and optical studies of Barium Titanate ( $BaTiO_3$ )

#### 3.2 Introduction

Barium Titanate (BaTiO<sub>3</sub>) is a perovskite oxide that has been widely studied for its structural and optical electronic properties[58], which are essential in electronic and photonic applications. This study examines two distinct forms of  $BaTiO_3$ .

In our study, we investigate the stability of the two possible forms  $[BaTiO_3]_1$  representing a single unit structure and  $[BaTiO_3]_c$  denoting a cubic form. (**Scheme 3.2**), geometry optimizations have been performed with a DFT approach .Then, TD-DFT computations have been carried out to assign the absorption and emission bands.



Scheme 3.2: Structures of BaTiO<sub>3</sub>

#### 3.3 Computational method

DFT calculations were carried out using the B3LYP, CAM-B3LYP, and M06-2X hybrid functional together with the LanL2DZ basis setaugmented with polarization functions on all atoms, except hydrogen ones[48].

The optimized geometry has been characterized as true minima on the potential energy surface using vibrational frequency calculations. Then, TDDFT calculations have been performed using the optimized geometry in order to compute the electronic spectra. The optimized geometries of the triplet excited states have been obtained using unrestricted methodology The program used for the DFT and TDDFT computations was Gaussian 09. Drawings of molecular

structures were done using the Mercury software,22 and molecular orbitals using GaussView23 program, whereas theoretical absorption spectra were plotted using Origin.

# 3.4 Structural electronic and optical studies of Barium Titanate [BaTiO<sub>3</sub>]<sub>1</sub>:

#### 3.4.1 structural properties:

Geometry optimization at the B3LYP/LANL2DZ and CAM-B3LYP/LANL2DZ levels in the gas phase, revealed for compound  $[BaTiO_3]_1$  which was proven to be minima in the potential energy surface by calculating the vibrational frequencies. The ground-state optimized structure of this compound is shown in **Figure 3.3**. Selected geometric parameters of the compound  $[BaTiO_3]_1$  at the different levels of computation are listed in **Table 3.1**.

The obtained optimized geometrie of  $[BaTiO_3]_1$ , using the B3LYP functional, are similar to those obtained using CAM-BLYP computations. In general, the optimized structural parameters in the  $S_0$  ground state are in good agreement with the X-ray structural analysis data . Slight differences between the calculated bond lengths, angles and Dihedral values and those given by the refinement of X-ray results are observed For example, the calculated Ti–O bond lengths were consistently shorter than the experimental values, with the CAM-B3LYP method yielding Ti–O distances of 1.792 Å and 1.675 Å compared to X-ray distances of 2.004 Å and 1.871 Å, respectively. Similarly, the Ba–Ti and Ba–O bond lengths were slightly underestimated, with B3LYP predicting 3.250 Å for Ba–Ti and 2.490 Å for Ba–O, whereas the experimental values were 3.427 Å and 2.877 Å. Furthermore, the bond angles are marginally compressed in the theoretical models. For instance, the Ba–Ti–O angle is calculated as 49.158°, which is significantly lower than the X-ray value of 56.985°, and the Ti–O–O angle is 41.434° compared to 45.125° experimentally.

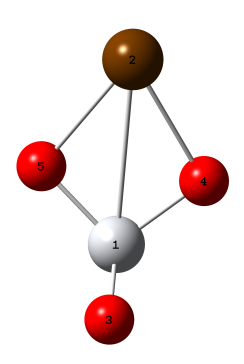


Figure 3.3: Optimized structures for ([BaTiO<sub>3</sub>]<sub>1</sub>) at the CAM-B3LYP/Lanl2DZ level of theory

Table 3.1: Selected experimental and theoretical structural parameters for [BaTiO<sub>3</sub>]<sub>1</sub>

	B3LYP LANL2DZ	CAM-B3LYP LANL2DZ	X-ray	REF
	The D	istance (Å)		
Ba2-O5	2.490	2.476	2.877	[54]
Ba2-Ti1	3.250	3.243	3.427	
O4-Ti1	1.807	1.792	2.004	
O3-Ti1	1.688	1.675	1.871	
	An	gles (°)		
Ba2-O5-O4	56.899	57.097	60.562	[54]
Ba2-Ti1-O4	49.464	49.158	56.985	
Ti1-Ba2-O5	33.498	33.234	35.759	
Ti1-O4-O5	41.251	41.434	45.125	

#### 3.4.2 Electronic properties:

In **Figure. 3.4** wish represent the molecular orbitals of [BaTiO<sub>3</sub>]<sub>1</sub> optimized for each Functional Hybrid and their HOMO-LUMO energy gaps.

In terms of electronic properties, the HOMO–LUMO energy gap was analyzed via molecular orbital visualization and energy calculations. Using B3LYP, the HOMO and LUMO energies were determined to be–4.378 eV and –3.163eV, respectively, resulting in a gap of 1.215 eV.

CAM-B3LYP produced HOMO and LUMO energies of –5.934 eV and –2.394 eV, with a narrower gap of 3.539eV. The character of frontier molecular orbitals, mainly HOMO (highest

occupied molecular orbital) and LUMO (lowest unoccupied molecular orbital) obviously influence the properties of the vertical electronic transitions. The HOMO is localized mainly on the Oxygen atoms. The lowest virtual orbitals are delocalized on the Barium and Oxygen atoms as illustrated on **Figure 3.4** It can be seen from this Figure that the large HOMO-LUMO energy gap values tend to have higher stability provided stability to the molecule.

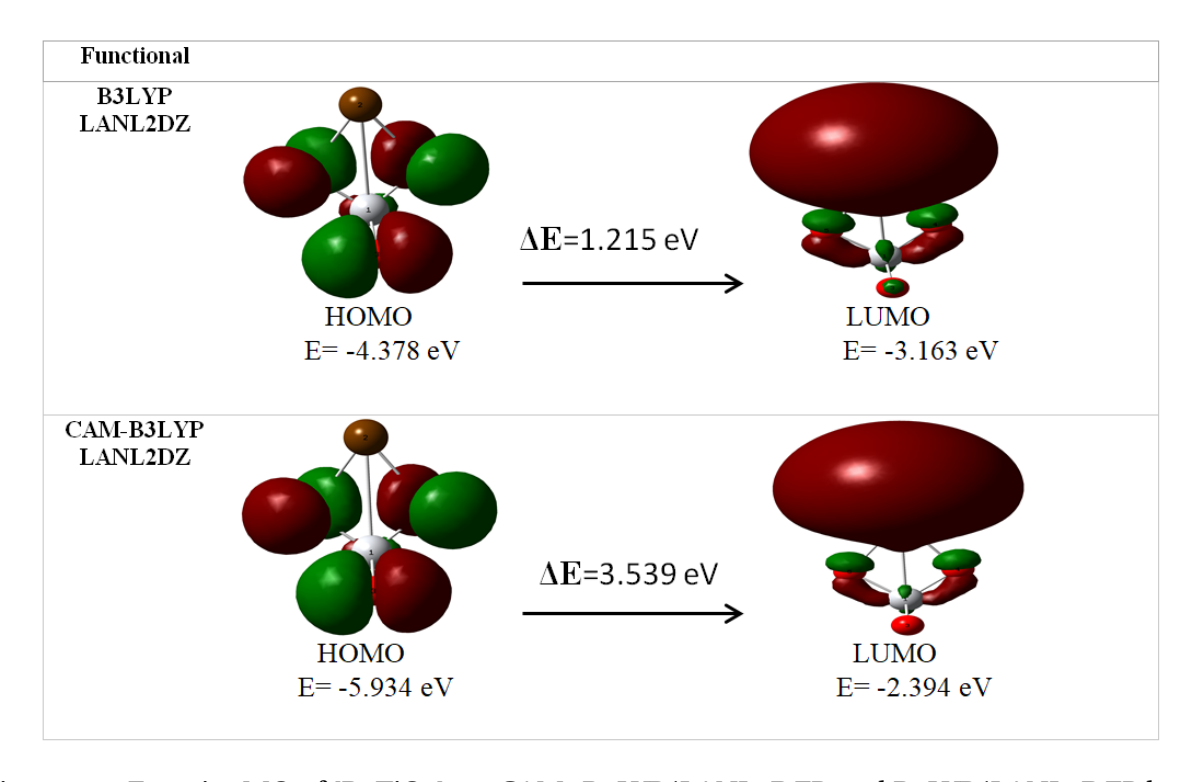


Figure 3.4: Frontier MO of [BaTiO<sub>3</sub>]<sub>1</sub> at CAM- B3LYP/LANL2DZP and B3LYP/LANL2DZP level .

#### 3.4.3 UV-Visible Spectroscopy of $[BaTiO_3]_1$ :

The calculated electronic transition energies and the corresponding oscillator strengths (f) of the low-lying singlet excited states for compound  $[BaTiO_3]_1$  with both B3LYP and CAM-B3LYP functionals are reported in **Table 3.2** and **Table 3.3**, the simulated spectra are depicted in **Figure 3.7.** 

#### • Time-Dependent DFT Analysis of [BaTiO<sub>3</sub>]<sub>1</sub> Using B3LYP functional:

To determine the nature of electronic transitions and the influence of electron-donating substituents on the UV-Visible absorption properties of the studied coordination systems, we carried out calculations based on time-dependent density functional theory (TD-DFT). We used

geometry optimizations of [BaTiO<sub>3</sub>]<sub>1</sub>. The results of excitation energy (E), wavelengths ( $\lambda$ ), and oscillator strength (f) of the transition are summarized in **Table 3.2**.

Experimentally, the UV–vis spectra of the BaTiO $_3$  present an intense band centered in the 330 nm [7], assigned to a O–Ba transition. The absorption band calculated with B3LYP Functional for [BaTiO $_3$ ] $_1$  compound is intense with a maximum very close to the to the visible region, at 388.82 nm (f = 0.113). In the case of this compound, the transition was O  $\rightarrow$  Ba, while it corresponds to HOMO -8  $\rightarrow$  LUMO (33%) and HOMO  $\rightarrow$  LUMO +2 (56%) (FIGURE 3.5).

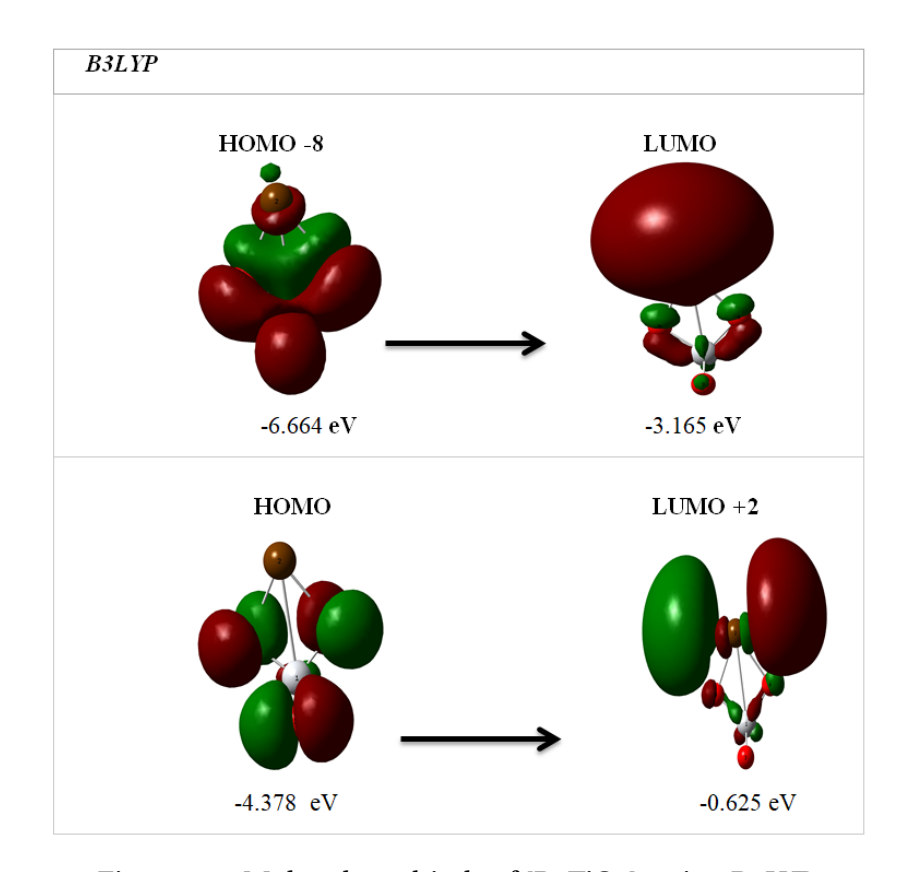


Figure 3.5: Molecular orbitals of [BaTiO<sub>3</sub>]<sub>1</sub>using B3LYP

Table 3.2: B3LYP results for [BaTiO<sub>3</sub>]<sub>1</sub>. E is the transition energy (in eV),  $\lambda_{cal}$  is the wavelength (in nm), and f is the oscillator strength of the excited state

Functional	$E_{\mathbf{exc}}$ (eV)	$\lambda_{\rm cal}$ (nm)	$\lambda_{\rm exp}$ (nm)	( <i>f</i> )	Transitional nature
B3LYP	3.19	388.82	330	0.113	33% HOMO–8 → LUMO 56% HOMO → LUMO+2

• Time-Dependent DFT Analysis of [BaTiO<sub>3</sub>]<sub>1</sub> Using CAM-B3LYP Functional:

**Table 3.3** shown the computed excitation energy ( $E_{\rm exc}$ ) of 3.766 eV corresponds to an absorption wavelength of 329.16 nm, placing BaTiO<sub>3</sub> within the ultraviolet range. Transition analysis revealed a dominant electronic redistribution of 50% from HOMO to LUMO +2, signifying the potential of the material in optoelectronic applications.

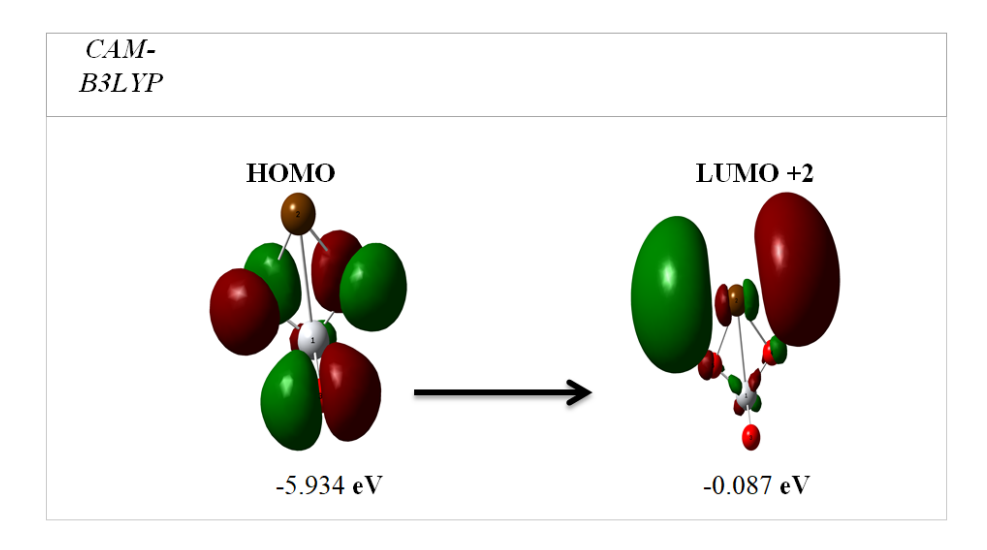


Figure 3.6: Molecular orbitals of [BaTiO<sub>3</sub>]<sub>1</sub> using CAM-B3LYP

Table 3.3: CAM-B3LYP results for  $[BaTiO_3]_1$ . E is the transition energy (in eV),  $\lambda_{cal}$  is the wavelength (in nm), and f is the oscillator strength of the excited state.

Functional	$E_{\mathbf{exc}}$ (eV)	$\lambda_{ extbf{max}}$	$\lambda_{ m exp}$	( <i>f</i> )	Transitional nature
CAM-B3LYP	3.766	329.16	330	0.036	50% HOMO → LUMO+2

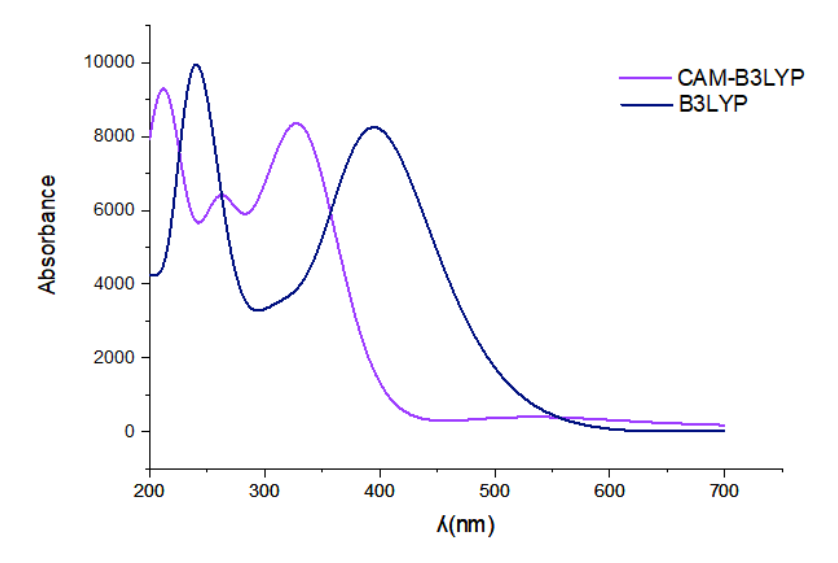


Figure 3.7: Simulated uvvis spectra of  $[BaTiO_3]_1$  at CAM-B3LYP/LANL2DZP and B3LYP/LANL2DZP level .

#### 3.4.4 IR Vibration Frequencies of [BaTiO<sub>3</sub>]<sub>1</sub>

The IR vibration frequencies were then calculated. The vibrational mode frequencies were calculated using molecular geometry optimization. This calculation is essential in all quantum computations, and aims to position the molecule at the minimum energy point on its molecular potential surface.

The Ba-(TiO3) vibrations can be treated by considering the TiO3 group as a single atom situated at the Ti position, and the vibrational problem that of a diatomic crystal of equivalent structure (e.g., the CsC1 structure). In the cubic phase, this will lead to a triply degenerate vibration since three equivalent axes exist.

The most characteristic IR vibrational frequencies calculated for the compounds, along with the experimental values, are presented in **Table 3.4** A comparative study between the calculated frequencies and those reported in the literature showed a very good agreement. This agreement confirmed the basic principle that the computational method can be adapted for similar calculations.

Table 3.4: Vibrational frequencies (in cm<sup>-1</sup>) in different functional and experimental values.

Mode	B3LYP	CAM-B3LYP	Exp
Ti-O	439.62	458.36	<b>495</b> <sup>[29]</sup>
Ti-O	790.51	824.39	<b>585</b> <sup>[20]</sup>
Ti-O	997	959.81	1440 <sup>[25]</sup>

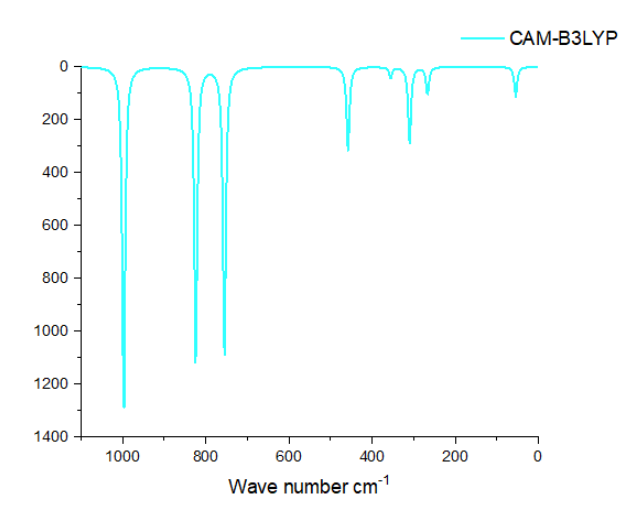


Figure 3.8: Simulated IR spectra of CAM-B3LYP for [BaTiO<sub>3</sub>]<sub>1</sub>

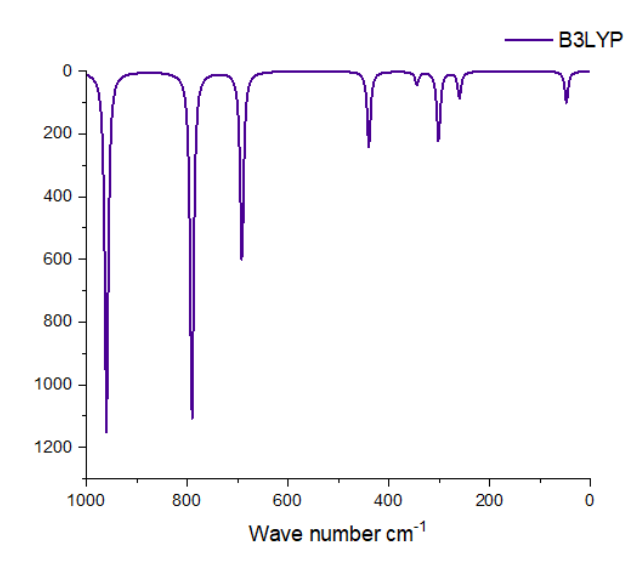


Figure 3.9: Simulated IR spectra of B3LYP for  $[BaTiO_3]_1$ 

## 3.5 Structural electronic and optical studies of Barium Titanate $[BaTiO_3]_c$ :

#### 3.5.1 Structural properties:

The structural analysis of BaTiO $_3$  in its [BaTiO $_3$ ] $_c$  based on computational optimization using the B3LYP, CAM-B3LYP, and M06-2X functionals with the LANL2DZ basis set revealed key atomic configurations influencing its electronic and optical behavior. The Ba-Ba interatomic distances range between 3.858 Å (M062X) and 5.460 Å (CAM-B3LYP), slightly deviating from the X-ray measured value of 5.654 Å, potentially due to computational relaxation effects. The Ti-O bond lengths remained relatively stable across different theoretical models, averaging 1.976–2.001 Å, compared to the experimental data of 2.135 Å. The bond angles further illustrate structural consistency, where Ba-O-Ba interactions maintain an approximately right-angle geometry ( $\sim$ 89.96°), whereas the O-Ba-O and Ti-Ba-Ba angles ranged between 54° and 61°, reflecting complex spatial arrangements **Table 3.5**.

The lattice stability and ionic interactions in  $BaTiO_3$  significantly contribute to its ferroelectric response, dielectric behavior, and potential optoelectronic applications, making structural characterization essential for understanding its material properties.

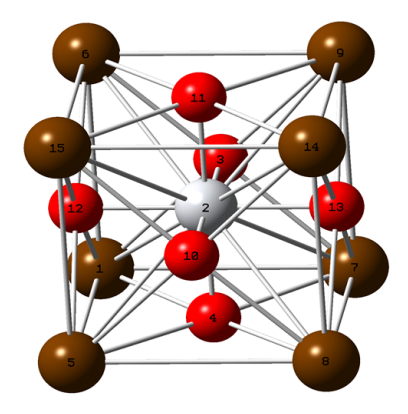


Figure 3.10: Optimized structures for ([BaTiO3]c) at the CAM-B3LYP/Lanl2DZ and B3LYP , M062X level of theory

Table 3.5: Selected experimental and theoretical structural parameters for [BaTiO<sub>3</sub>]<sub>c</sub>

	B3LYP LANL2DZ	CAM-B3LYP LANL2DZ	M06-2X LANL2DZ	X-ray	REF
	Tł	ne Distance (Å)			
Ba15-Ba14	3.893	3.860	3.858	5.654	[54]
Ba5-Ba14	5.506	5.460	5.456	5.654	
Ti2-O3	2.000	1.976	1.977	2.135	
Ti2-O11	2.001	1.977	1.977	2.135	
		Angles (°)			
Ba15-O10-Ba14	89.958	89.961	89.964	83.699	[54]
O10-Ba5-O4	61.839	61.585	61.649	61.548	
Ti2-Ba8-Ba7	54.735	54.732	54.725	55.408	
O11-Ba14-Ba9	45.040	45.006	45.050	44.941	

#### 3.5.2 Electronic properties:

The electronic properties of [BaTiO<sub>3</sub>]<sub>c</sub> were evaluated using density functional theory (DFT) calculations with B3LYP, CAM-B3LYP, and M06-2X functionals employing the LANL2DZ basis set to analyze the highest occupied molecular orbital (HOMO) and lowest unoccupied molecular orbital (LUMO) distributions. The HOMO-LUMO gap varies across functionals, with values of 0.750 eV (B3LYP), 1.800 eV (CAM-B3LYP), and 1.568 eV (M06-2X), as illustrated in Figure 3.11, indicating differences in the charge transfer efficiency and optical absorption potential. The smaller gap obtained with B3LYP suggests semiconducting behavior suitable for electronic applications, whereas CAM-B3LYP predicts improved excitonic stability, making it favorable for optoelectronic materials. The variation in the energy levels highlights the dependence of [BaTiO<sub>3</sub>]<sub>c</sub> electronic properties on computational approaches, impacting its dielectric response, ferroelectric behavior, and optical performance.

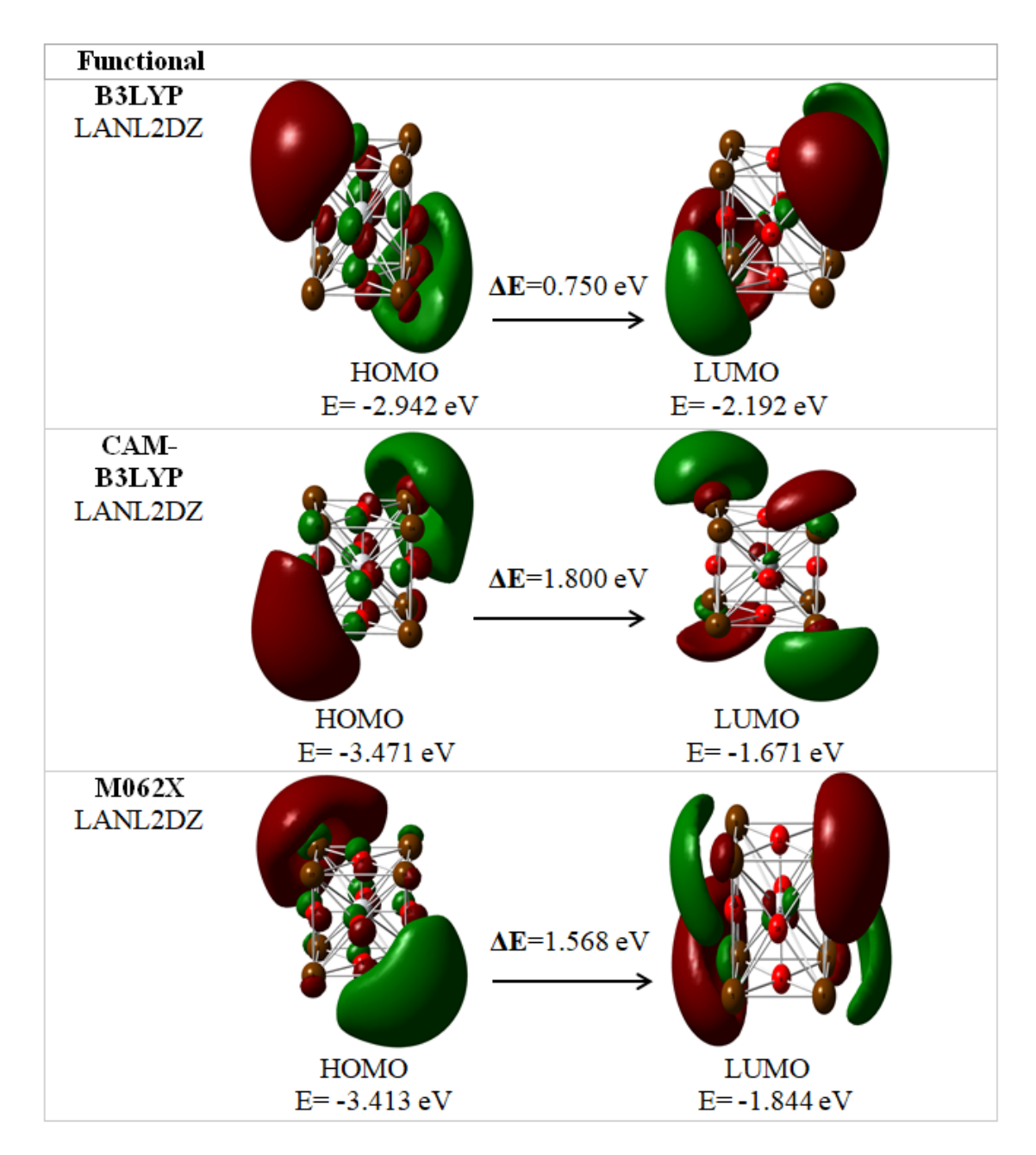


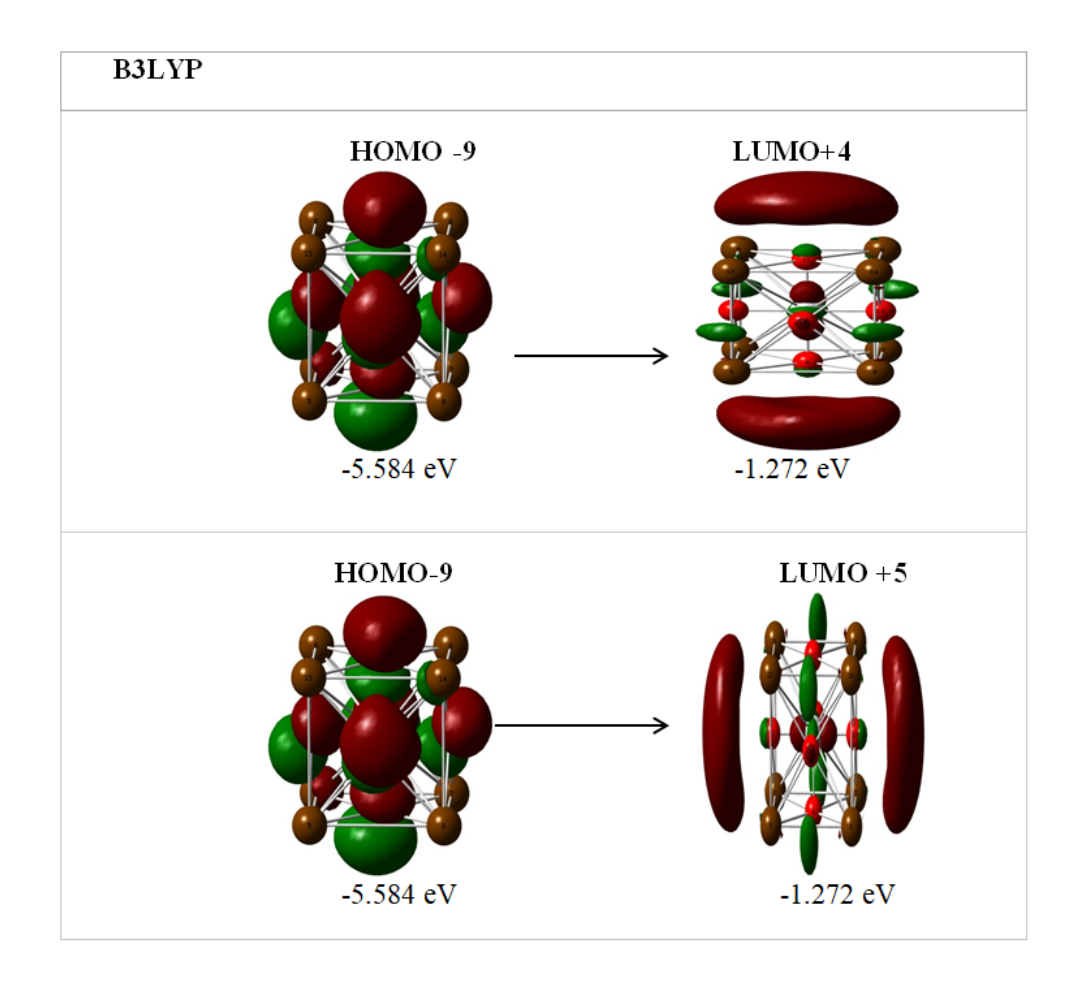
Figure 3.11: Frontier MO of  $[BaTiO_3]_c$  at CAM- B3LYP/LANL2DZP , B3LYP/LANL2DZP and M062X/LANL2DZ level

#### 3.5.3 UV-Visible Spectroscopy of [BaTiO<sub>3</sub>]<sub>c</sub>:

#### • Time-Dependent DFT Analysis of [BaTiO<sub>3</sub>]<sub>c</sub> Using B3LYP Functional:

The optical properties of the  $BaTiO_3$  complex were studied by time-dependent DFT (TD-DFT) calculations using the B3LYP functional. The absorption spectrum shows a prominent

peak at a wavelength of **328.78 nm**, which corresponds to an excitation energy ( $E_{\rm exc}$ ) of **3.771 eV**. This transition is attributed to a combination of multiple electronic excitations, predominantly from the deeper occupied orbitals (HOMO–9, HOMO–8, and HOMO–7) to the unoccupied orbitals (LUMO+4 and LUMO+5). Specifically, the transitions contributing to this absorption are 10% HOMO–9  $\rightarrow$  LUMO+4, 32% HOMO–9  $\rightarrow$  LUMO+5, 32% HOMO–8  $\rightarrow$  LUMO+4, and 32% HOMO–7  $\rightarrow$  LUMO+5. The oscillator strength (f) of **0.235** indicates a moderately allowed transition, which reflects the considerable probability of photon absorption at this wavelength. The distribution of charge density across these transitions implies notable charge transfer within the structure, which supports the semiconducting and optoelectronic potential of BaTiO<sub>3</sub>.



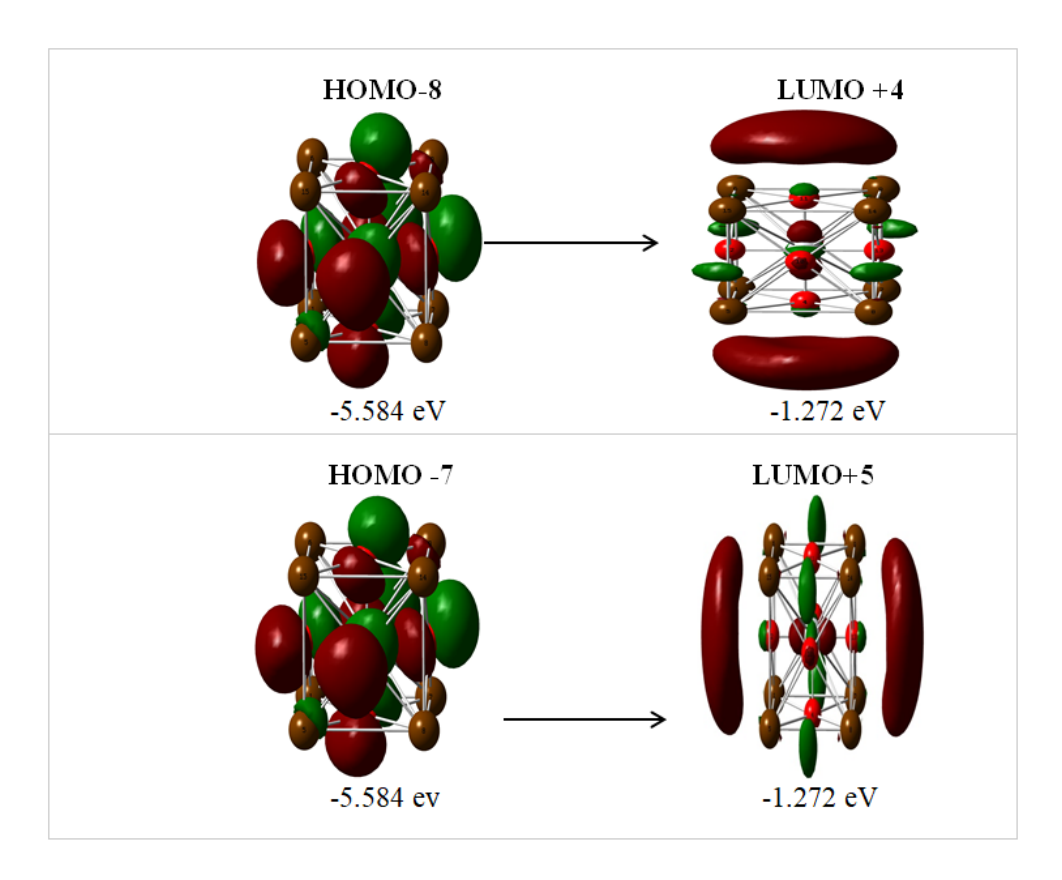


Figure 3.12: Molecular orbitals of [BaTiO<sub>3</sub>]<sub>c</sub> using B3LYP

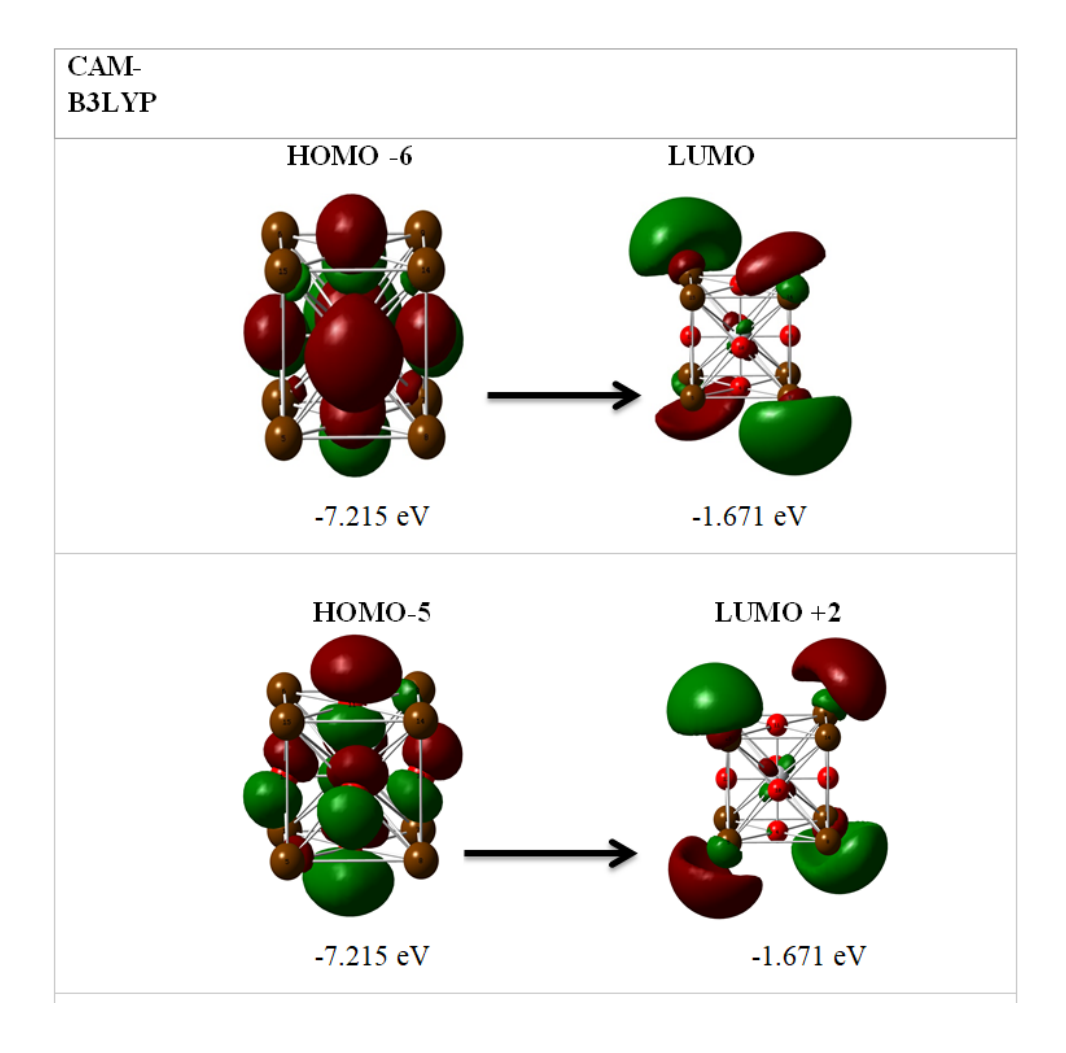
Table 3.6: B3LYP results for  $[BaTiO_3]_c$ . E is the transition energy (in eV)  $\lambda_{cal}$  (nm) and f is the oscillator strength of the excited state.

Functional	$E_{\mathbf{exc}}$ (eV)	$\lambda_{\rm cal}$ (nm)	$\lambda_{\rm exp}$ (nm)	f	Transitional nature
ВЗІУР	3.771	328.78	330	0.235	$10\% \text{ HOMO}-9 \rightarrow \text{LUMO}+4$ $32\% \text{ HOMO}-9 \rightarrow \text{LUMO}+5$ $32\% \text{ HOMO}-8 \rightarrow \text{LUMO}+4$ $32\% \text{ HOMO}-7 \rightarrow \text{LUMO}+5$

#### • Time-Dependent DFT Analysis of [BaTiO<sub>3</sub>]<sub>c</sub> Using CAM-B3LYP Functional

The optical properties of the [BaTiO<sub>3</sub>]<sub>c</sub> were studied by time-dependent DFT (TD-DFT) calculations using the CAM-B3LYP functional. The absorption spectrum shows a prominent peak at a wavelength of **328.03 nm**, which corresponds to an excitation energy ( $E_{\rm exc}$ ) of **3.779 eV**. The transitions contributing to this absorption were 29% HOMO-6  $\rightarrow$  LUMO, 15% HOMO-7  $\rightarrow$  LUMO+2, 19% HOMO-4  $\rightarrow$  LUMO, and 25% HOMO-7  $\rightarrow$  LUMO+2. An oscillator strength (f) of **0.203** indicates a moderately allowed transition, which reflects a considerable probability of

photon absorption at this wavelength. The distribution of charge density across these transitions implies notable charge transfer within the structure, which supports the semiconducting and optoelectronic potential of  $BaTiO_3$ .



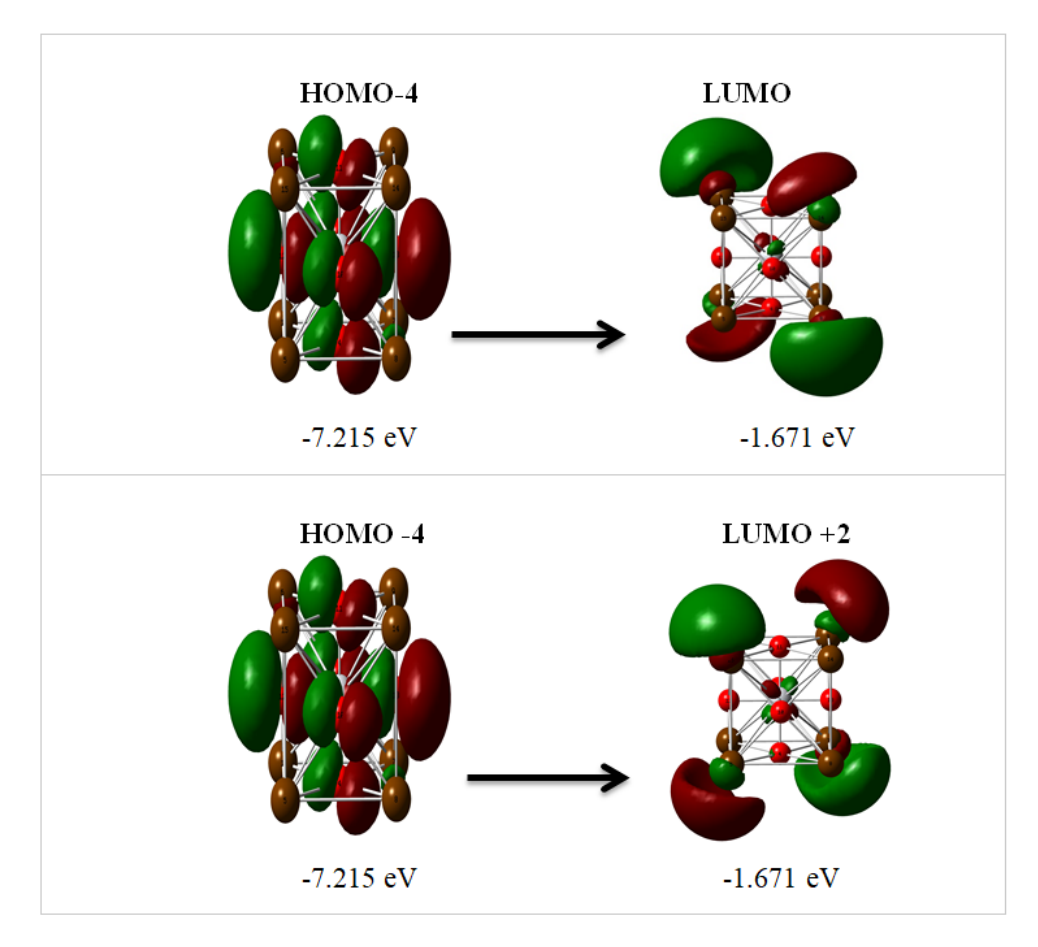


Figure 3.13: Molecular orbitals of [BaTiO<sub>3</sub>]<sub>c</sub> using CAM-B3LYP

Table 3.7: CAM-B3LYP results for  $[BaTiO_3]_c$ . E is the transition energy (in eV)  $\lambda_{cal}$  (nm) and f is the oscillator strength of the excited stat

Functional	E <sub>exc</sub> (eV)	$\lambda_{\rm cal}$ (nm)	$\lambda_{\rm exp}$ (nm)	f	Transitional nature
CAM-B3LYP	3.779	328.03	330	0.203	29% HOMO-6 → LUMO 15% HOMO-7 → LUMO+2 19% HOMO-4 → LUMO 25% HOMO-4 → LUMO+2

#### • Time-Dependent DFT Analysis of [BaTiO<sub>3</sub>]<sub>c</sub> Using M06-2X Functional

The optical properties of the BaTiO<sub>3</sub> complex were investigated using the M06-2X functional, revealing significant insights into its electronic excitation behavior. The calculated excitation energy ( $E_{\rm exc}$ ) was 3.735 eV, corresponding to an absorption wavelength of 331.92 nm. An oscillator strength (f) of 0.051 indicated a weakly allowed electronic transition. Notably, the

transition is primarily composed of two contributions: 15% from HOMO-3 to LUMO+17 and 34% from HOMO-3 to LUMO+18, suggesting the involvement of deeper-lying occupied orbitals and higher unoccupied orbitals rather than simple HOMO-LUMO excitation. This reflects the complex nature of charge transfer within the molecule. Furthermore, molecular orbital analysis shows an energy separation of approximately 0.175 eV between the involved orbitals (from -0.162 eV to +0.013 eV), highlighting the electronic delocalization and structural interactions contributing to the absorption behavior of the complex.

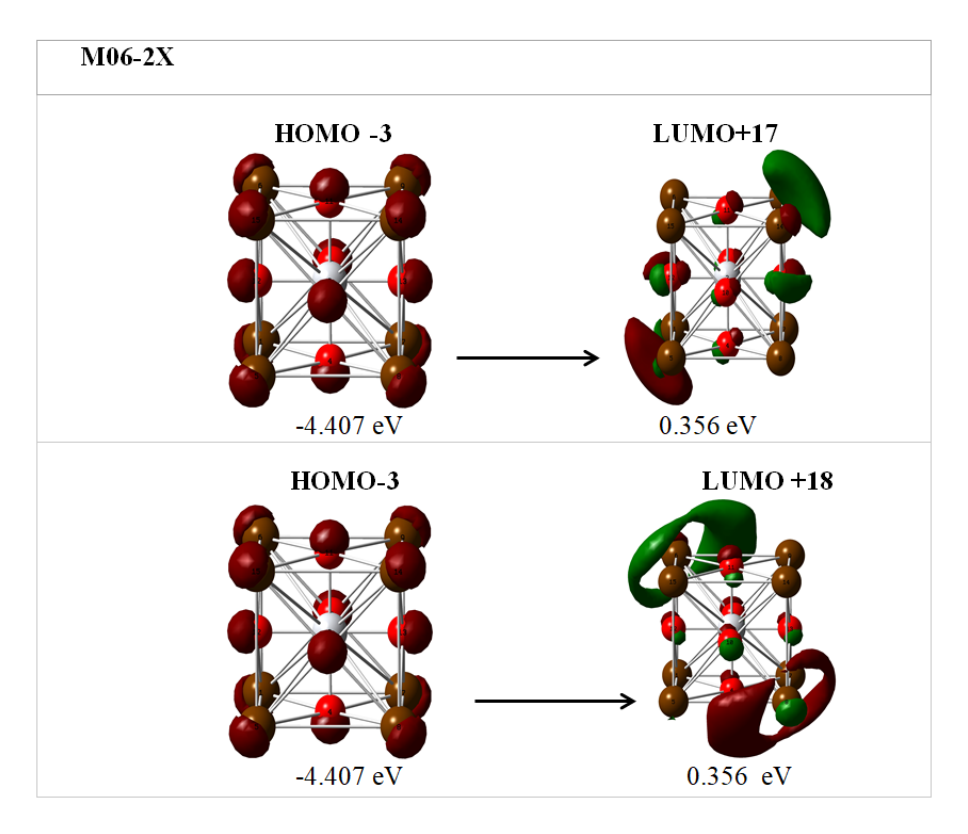


Figure 3.14: Molecular orbitals of [BaTiO<sub>3</sub>]<sub>c</sub> using M06-2X

Table 3.8: M06-2X results for  $[BaTiO_3]_c$ . E is the transition energy (in eV)  $\lambda_{cal}$  (nm) and f is the oscillator strength of the excited stat

Functional	$E_{\mathbf{exc}}$ (eV)	$\lambda_{\rm cal}$ (nm)	$\lambda_{\rm exp}$ (nm)	f	Transitional nature
M06-2X	3.735	331.92	330	0.051	15% HOMO-3 → LUMO+17 34% HOMO-3 → LUMO+18

 $\bullet$  Among the tested functionals, CAM-B3LYP applied to the [BaTiO3]1 structure demonstrated the closest match to the experimental UV-Vis absorption data, predicting a maximum.

mum absorption at 329.16 nm with a minimal deviation of -0.84 nm from the experimental value (330 nm). M06-2X also showed reliable accuracy, yielding a predicted absorption at 331.92 nm (deviation of +1.92 nm). For the complex forms of BaTiO<sub>3</sub>, both CAM-B3LYP and B3LYP predicted slightly higher excitation energies, indicating blue-shifted behavior under idealized conditions. In terms of the oscillator strength, the B3LYP functional applied to the [BaTiO<sub>3</sub>]<sub>c</sub> exhibited the highest value (0.253), suggesting stronger light absorption and better charge mobility. Conversely, M06-2X, which is highly stable owing to its low oscillator strength (0.051), may be less favorable for optoelectronic applications requiring high excitability. Therefore, CAM-B3LYP was identified as the most accurate functional for simulating the experimental UV-Vis spectra, while B3LYP (of [BaTiO<sub>3</sub>]<sub>c</sub>) stands out for enhancing the optical transition intensity and charge transport behavior.

Table 3.9: Comparison of calculated absorption parameters using different functionals and structures with the experimental absorption peak at 330 nm.

Peak Shift (vs.	Oscillator	Absorption	Excitation	Functional	Structure
Experimental 330 nm)	Strength (F)	Wavelength (nm)	Energy (E <sub>exc</sub> ) (eV)		
Red-shifted (+58.82 nm)	0.113	388.82 nm	3.19 eV	B3LYP	[BaTiO <sub>3</sub> ] <sub>1</sub>
Closest match (-0.84 nm)	0.036	329.16 nm	3.766 eV	CAM-B3LYP	$[BaTiO_3]_1$
Closest match (+1.92 nm)	0.051	331.92 nm	3.735 eV	M06-2X	[BaTiO <sub>3</sub> ] <sub>c</sub>
Blue-shifted (-1.97 nm)	0.203	328.03 nm	3.779 eV	CAM-B3LYP	$[BaTiO_3]_c$
Blue-shifted (-1.22 nm)	0.235	328.78 nm	3.771 eV	B3LYP	$[BaTiO_3]_c$

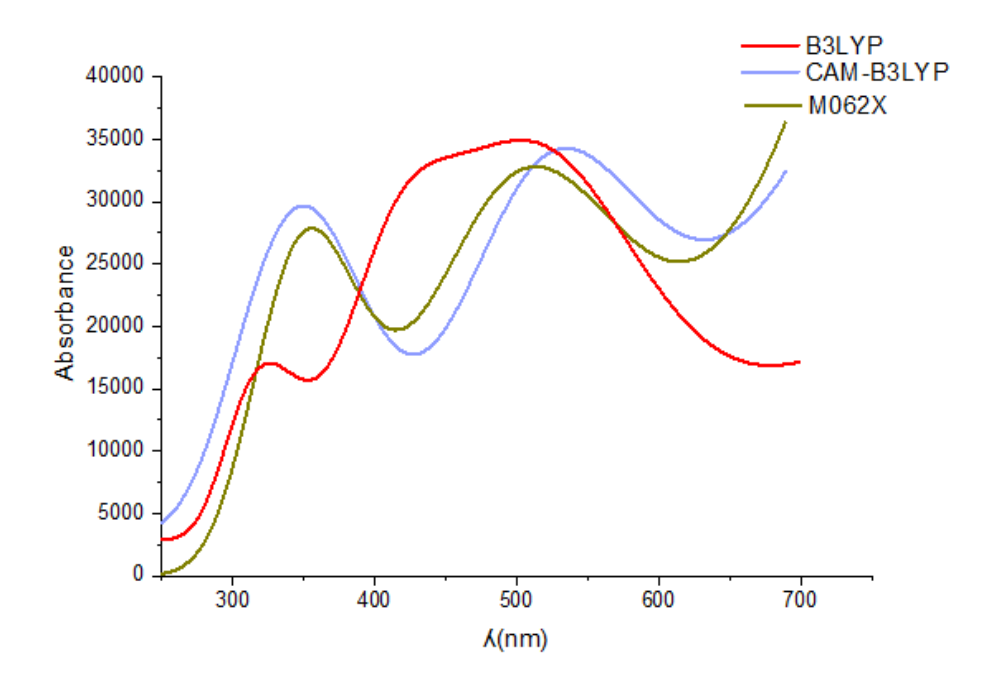


Figure 3.15: Simulated UV-visible spectra of CAM-B3LYP , B3LYP and M062X of  $BaTiO_3$ 

#### 3.5.4 IR Vibration Frequencies of [BaTiO<sub>3</sub>]<sub>c</sub>

The most characteristic IR vibration frequencies calculated for  $[BaTiO_3]_c$ , along with the experimental values obtained by other researchers, are compiled in **Table 3.10**. The displayed results reveal that the experimental and calculated values are approximately close.

Table 3.10: Vibrational frequencies (in cm<sup>-1</sup>) in different functional and experimental values.

Mode	B3LYP	CAM-B3LYP	M062X	Exp
Ti-O	415.30	433.37	430.26	<b>495</b> <sup>[29]</sup>
Ti-O	382.50	352.62	382.50	<b>585</b> <sup>[20]</sup>

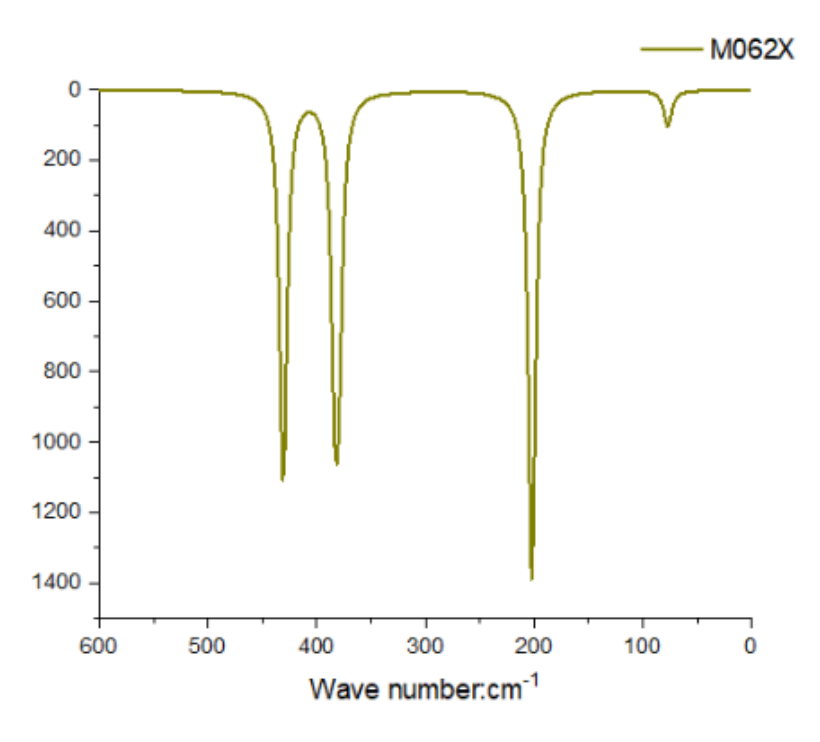


Figure 3.16: Simulated IR spectra of M062X for  $[BaTiO_3]_c$ 

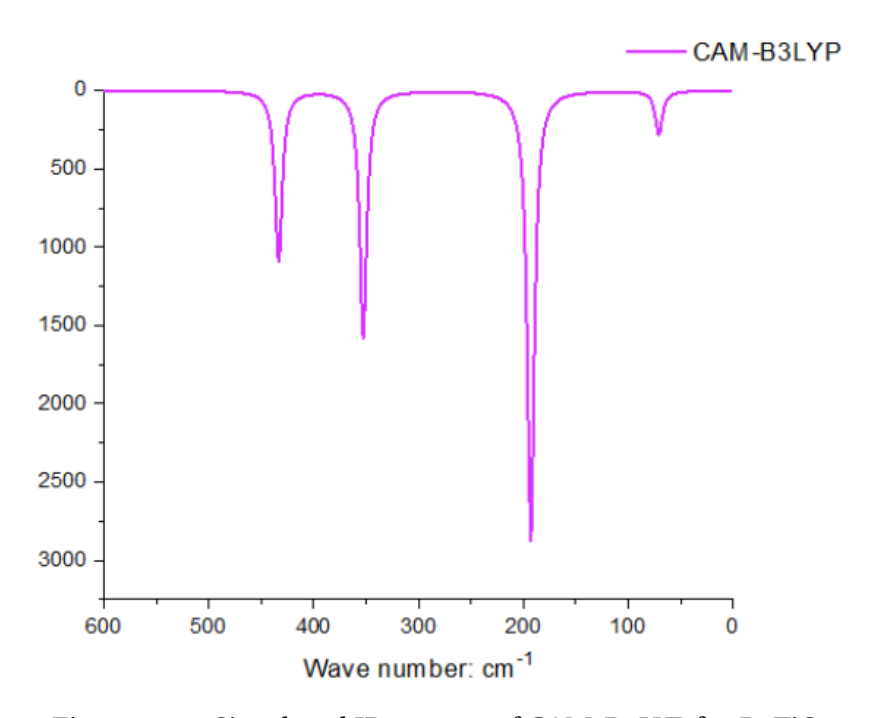


Figure 3.17: Simulated IR spectra of CAM-B3LYP for  $BaTiO_{3c}$ 

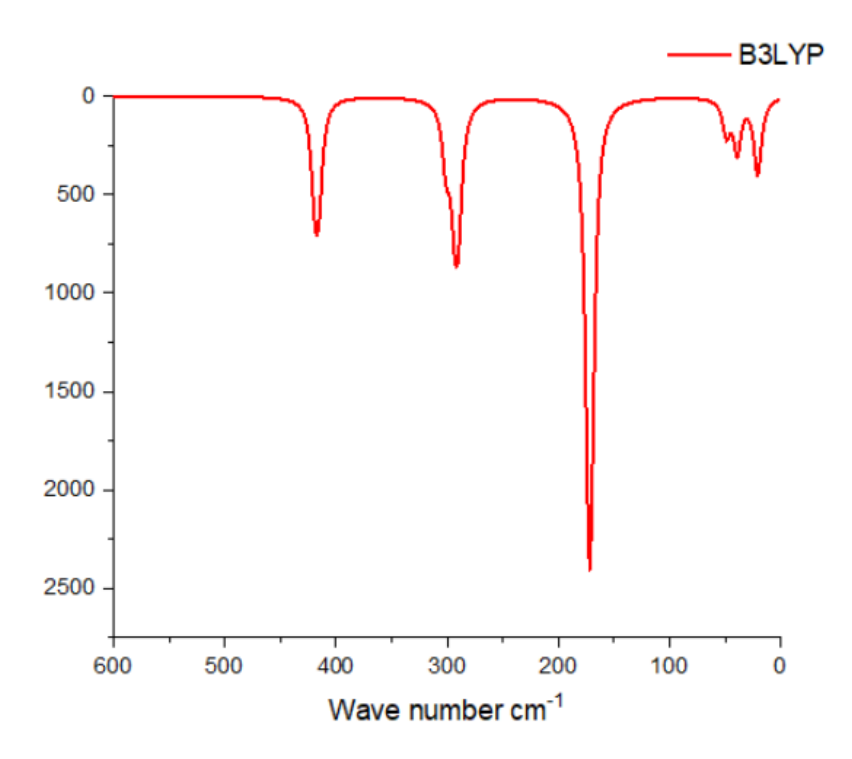


Figure 3.18: Simulated IR spectra of B3LYP for  $[BaTiO_3]_c$ 

### Part II

# Structural electronic and optical studies of $BaTiO_3/PEG$

#### 3.6 Introduction

Hybrid nanocomposites have concerned significant research attention in recent years due to their unique properties, including their structure, interaction with light (optical properties )[2] Combining one or more metal oxide nanoparticles (BaTiO<sub>3</sub>) with one or more polymer composite (PEG) leads to a new class of state-of-art nanocomposites. polyethylene glycol (PEG) is a highly water soluble and nontoxic material; besides, its solubility in most organic solvents is considerably high[24][25]. This work aims to design of new PEG/BaTiO<sub>3</sub> nanostructures combining between the properties of PEG and BaTiO<sub>3</sub> nanostructures to create new material used as a key for different electronics fields. To investigate the possible existence of PEG/BaTiO<sub>3</sub> nanostructures.

## 3.7 Structural electronic and optical studies of polyethylene glycol (PEG):

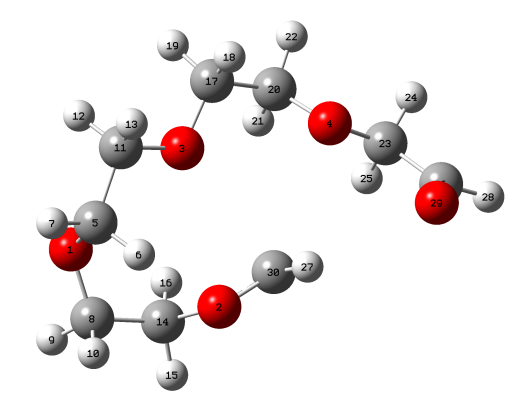


Figure 3.19: the PEG optimized molecule for CAM/B3LYP.

#### 3.7.1 Structural properties of PEG:

The structural properties of polyethylene glycol (PEG) were investigated using density functional theory (DFT) at the CAM-B3LYP/6-311g(d,p) level, and the results were compared with available X-ray crystallographic data. [9] The optimized geometry revealed a flexible, non-planar

conformation characteristic of PEG because of its ether linkages and repeating –CH<sub>2</sub>–CH<sub>2</sub>–Ounits. Key bond lengths, such as C–O and C–H, were found to be 1.294 Å and 1.092 Å, respectively, which are close to the experimental values (1.440 Å and 0.970 Å), indicating the reliability of the computational method. Similarly, the O–C–C and H–C–H bond angles **Table 3.11** were within acceptable deviations, supporting the conformational accuracy of the model. A comparison between the optimized and non-optimized geometries illustrates that optimization significantly reduces steric hindrance and results in a more stable, folded molecular structure. These structural features confirm PEG's intrinsic flexibility of PEG and its ability to adopt low-energy conformations, which are critical for its solubility, biocompatibility, and applications in drug delivery and materials science.

Table 3.11: Selected experimental and theoretical structural parameters for PEG

	CAM-B3LYP /6-311g(d,p	X-ray	REF				
	The Distance (Å)						
C30-O2	1.294	1.440	[9]				
C17-O4	2.373	2.415					
C8-H9	1.092	0.970					
C11-H13	1.100	0.969					
	Angles (°)						
C26-C23-O29	23.880	32.026	[9]				
C17-H19-H18	35.813	35.897					
O3-C11-C17	32.917	34.369					

#### 3.7.2 Electronic properties:

The electronic properties of polyethylene glycol (PEG) were investigated using the CAM-B3LYP functional with the 6-311g(d,p) basis set. The calculated energy of the highest occupied molecular orbital (HOMO) was found to be –7.160 eV, while the energy of the lowest unoccupied molecular orbital (LUMO) was 0.653 eV. This results in a significantly large HOMO–LUMO energy gap of 7.813 eV, indicating a high degree of electronic stability and suggesting that PEG behaves as an insulator. The molecular orbital distribution shows that both HOMO and LUMO are primarily localized over the ether functional groups along the PEG backbone, with the HOMO concentrated on oxygen and adjacent carbon atoms, while the LUMO exhibits antibonding

character over similar regions. The large energy gap also implies weak electronic transitions under normal conditions, making PEG less responsive in optoelectronic applications but highly suitable for use as a dielectric material or a stabilizing agent in nanocomposite systems.

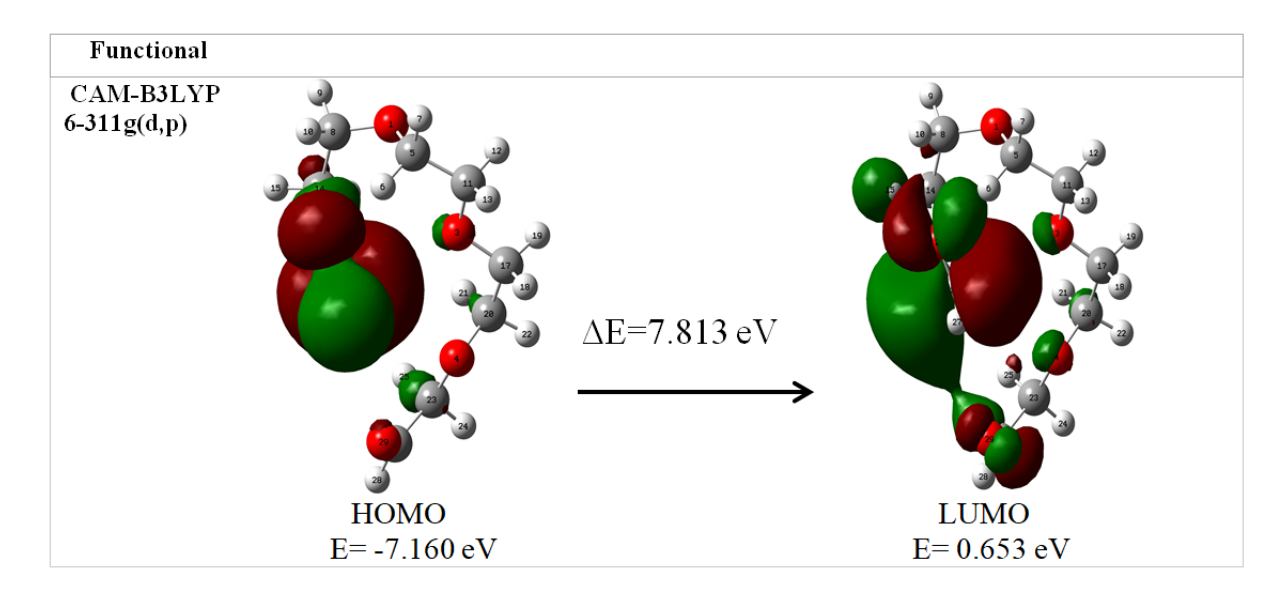


Figure 3.20: Frontier MO of PEG

#### 3.7.3 UV-vis spectroscopy

#### • Time-Dependent DFT Analysis Using CAM-B3LYP Functional

The theoretical UV-Vis absorption spectrum of polyethylene glycol (PEG), calculated using (TD-DFT), shows a maximum absorption at approximately 189 nm. This value corresponds to the intrinsic electronic transition of the ether groups in the PEG backbone. Experimentally, however, the reported of maximum absorption for PEG is often around 212 nm [52]. This discrepancy is attributed to various environmental and experimental factors, including the presence of water molecules trapped within the polymer matrix, intermolecular interactions, and the limitations of spectrophotometers that typically do not measure below 190–200 nm. Therefore, the computational result at 189 nm reflects the true electronic behavior of the isolated PEG molecule, whereas the experimental shift to 212 nm results from real-world measurement condition. The transition primarily involves electron excitation from HOMO-2 to the LUMO (64%), Table 3.12, reflecting the molecular orbital contributions to its optical behavior. These

properties are significant for PEG's potential applications of PEG in optoelectronics, drug delivery, and biocompatible coatings, where controlled UV absorption can influence its functionality.

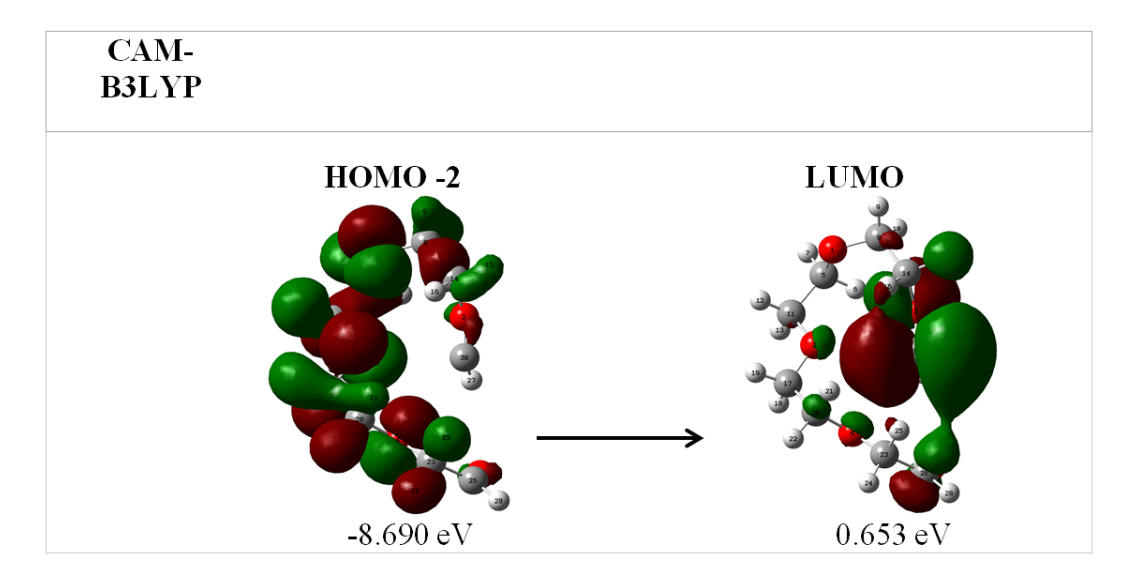


Figure 3.21: Molecular orbitals of PEG using CAM-B3LYP.

Table 3.12: Absorption characteristics of the PEG

Functional	$E_{\rm exc}$ (eV)	$\lambda_{\rm cal}$ (nm)	$\lambda_{\mathrm{Exp}}$ (nm)	F	Transitional nature
CAM-B3LYP	6.560	189.00	212	0.010	64% HOMO-2 → LUMO

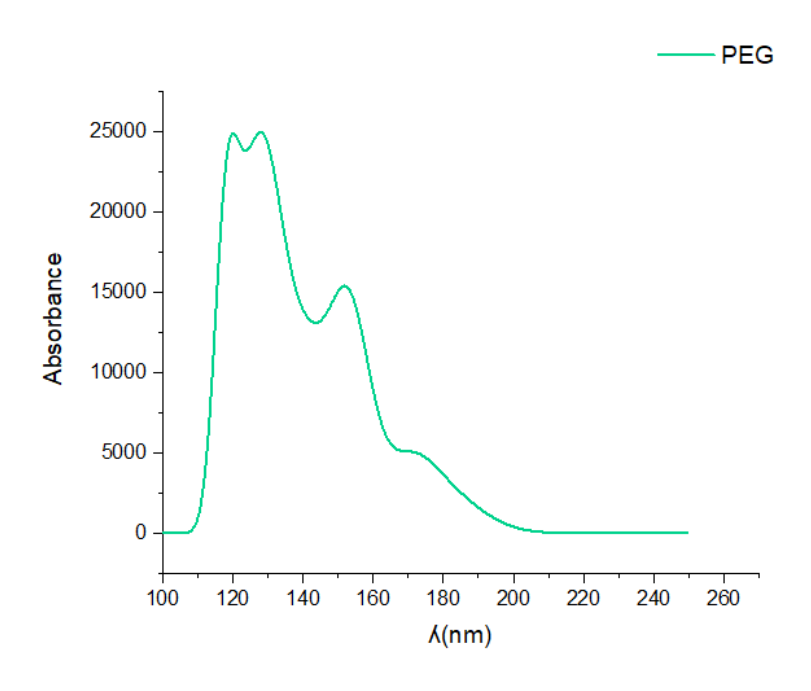


Figure 3.22: Simulated UV-visible spectra of PEG.

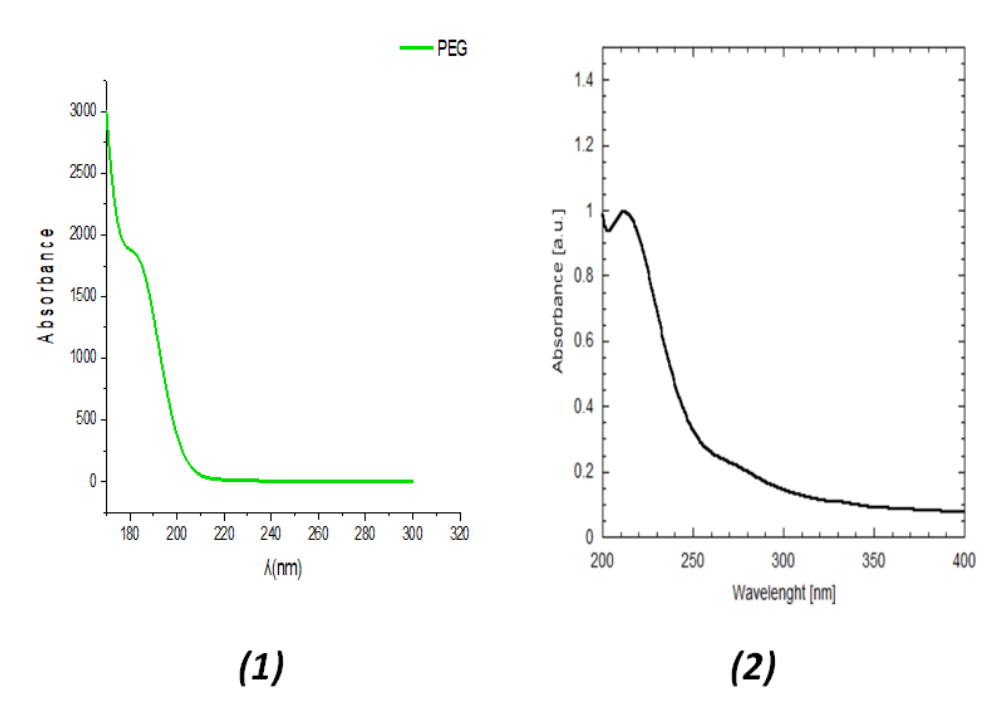


Figure 3.23: UVvisible spectra of PEG (1):TDDFT and (2):Experimentally.

#### 3.7.4 IR Vibration Frequencies:

In terms of polyethylene glycol (PEG), its distinctive peak arises from the symmetric stretching vibrations of the methylene group, observed at 2890.42 (cm $^{-1}$ ). The antisymmetric stretching vibration of the methylene group is observed at 3003 (cm $^{-1}$ ). The band at 1370.88 (cm $^{-1}$ ) corresponds to the symmetric bending mode of the CH $_2$ -CH $_2$  group, while the bands at 1370.88 (cm $^{-1}$ ) represent the CH $_2$  twisting vibrations. Furthermore, the C-O stretching and CH2 rocking vibrations are evident at 1197 (cm $^{-1}$ ) corresponds a strong peak in PEG due to ether group

Table 3.13: Vibrational frequencies (in cm<sup>-1</sup>) in different functional and experimental values of PEG.

Bond	Exp (cm <sup>-1</sup> )	Calculated peak cm <sup>-1</sup>	Assignment
С-Н	3079	3027.09	peak likely corresponds to the stretching of C–H bonds in the methylene (–CH <sub>2</sub> –) groups that make up the polymer backbone of PEG. $^{[8]}$
C–H (CH <sub>2</sub> )	2880-2950	2890.42	stretching from methylene groups $^{[40]}$
С–Н	1340–1370	1370.88	out-of-plane deformation [40]
C-O-C	1100–1145	1197	strong peak in PEG due to ether bond [53]
С-О-Н	1700–1750	1873.68	strong peak in PEG due to ether group [8]

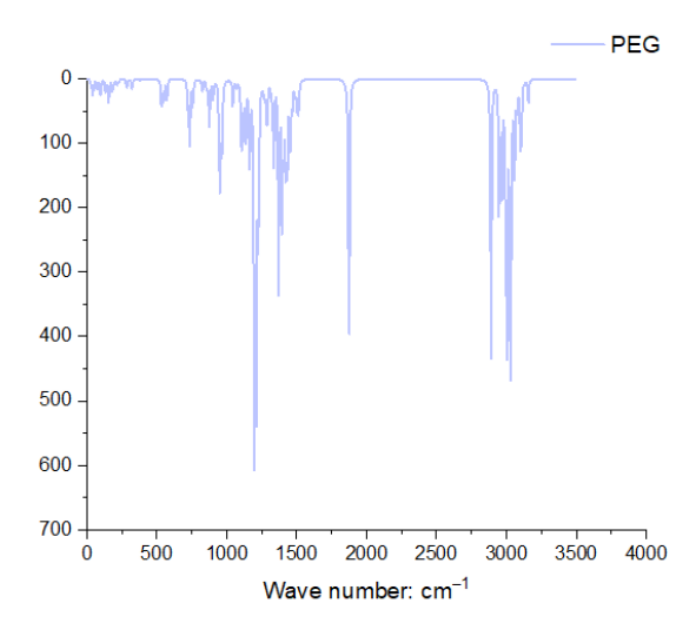


Figure 3.24: Simulated IR spectra OF PEG.

### 3.8 Structural electronic and optical studies of $BaTiO_3/PEG$ :

This research focuses on the development of novel **PEG/BaTiO**<sub>3</sub> **nanocomposites** by leveraging the synergistic properties of polyethylene glycol (PEG) and BaTiO<sub>3</sub> nanoparticles. By combining the flexibility, biocompatibility, and functional versatility of PEG with the ferroelectric

and optical properties of  $BaTiO_3$ , this study aims to create advanced materials for diverse applications in electronics and optoelectronics. The designed nanocomposite is envisioned to be a key component in emerging technologies, providing enhanced structural stability, electrical performance, and adaptability to different environmental conditions.

#### 3.8.1 Modelling of the BaTiO<sub>3</sub>/PEG nanocomposite

The primary objective is to predict the precise structural model of the newly developed **BaTiO**<sub>3</sub>/**PEG** hybrid material and comprehensively analyze its properties, including the structural arrangement, optoelectronic behavior, and chemical reactivity descriptors.

This study provides deep insights into the geometric characteristics of nanocomposites, such as atomic distribution, bond lengths, and dihedral angles, which contribute to understanding their interaction mechanisms and potential effects in optical and electronic applications. In addition to the diverse experimental analysis methods employed to examine the novel BaTiO<sub>3</sub>/PEG composite and related properties, complementary theoretical calculations based on density functional theory (DFT) [6] using the Becke three-parameter Lee-Yang-Parr (CAM-B3LYP) functional [31] [6] with the basis set lanl2dz were conducted in this study. This approach aims to predict the structural and vibrational measurements, as well as to understand the structure–property relationships of the formed nanocomposite, including the optoelectronic properties and quantum chemical parameters related to its chemical reactivity.

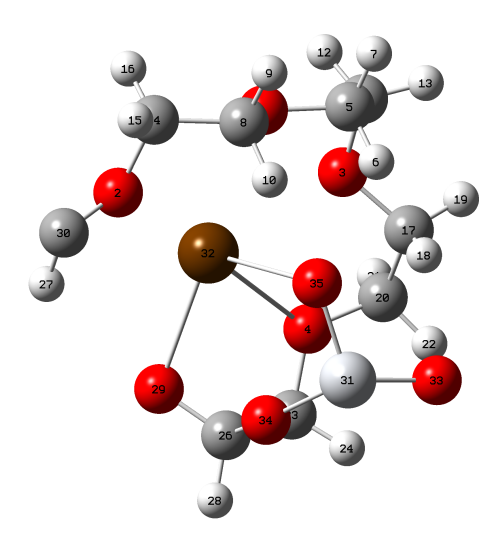


Figure 3.25: the BaTiO<sub>3</sub>/PEG optimized molecule for CAM/B3LYP DFT calculation.

#### 3.8.2 Structural properties of the BaTiO<sub>3</sub>/PEG nanocomposite:

As clearly shown from the optimized structure, that there is a formation of new chemical liaison between the barium atom (Ba32) of BaTiO<sub>3</sub> and the 2 oxygen atoms (O4) and (O29) of polyethylene glycol, which can interpret as a chemical reaction between the two substances. It is well-known that the BaTiO<sub>3</sub> has a high affinity for calcium ions and can form strong ionic bonds with them. Therefore, in this case of BaTiO<sub>3</sub> and PEG, the interaction is more likely to be dominated by ionic bonding between the barium cation of BaTiO<sub>3</sub> and the oxygen anion of PEG. This is because barium and oxygen have significantly different electronigativities, which results in a large difference in their electron densities and strong attraction between them. The bond lengths between Barium ions of BaTiO<sub>3</sub> and oxygen of PEG are approximately equal to the sum of van der Waals radii of these atoms. As shown in **Table 3.14**, these bond lengths are in the range of 2.589 Å and 2.684 Å and correlated toto the theoretical bond lengths of the new

chemical liaison Ba32-O4.

Table 3.14: Bond lengths and angles of PEG/BaTiO<sub>3</sub> nanostructure.

Measurements Optimization parameters		Values
	(Ba32-O35)	2.696
	(C17–O4)	2.396
	(Ba32–O29)	2.589
Bonds, Å	(O2–H27)	1.940
	(Ba32–Ti31)	3.503
	(Ba32–C20)	3.712
	(Ba32–O4)	2.684
	(Ba32-C26-H28)	159.541
Angles, deg.	(Ba32-O29-O4)	59.770
	(Ba32-O35-O34)	65.863
	(Ti31–O35–Ba32)	102.139

#### 3.8.3 Frontier molecular orbitals (FMOs)

The frontier molecular orbital (MO) diagrams are shown in Figure 3.26

The HOMO orbital has an energy of -6.211 eV and the LUMO orbital with an energy of -1.149 eV. . The highest value of the HOMO orbital is attributed to the oxygen electron donating groups, while the drop in LUMO value is due to the Barium atom. The HOMO is localized mainly on the the Ba atom. The lowest virtual orbitals are delocalized on the the O atoms. It can be seen from this Figure that the large HOMO-LUMO energy gap values tend to have higher stability provided stability to the system.

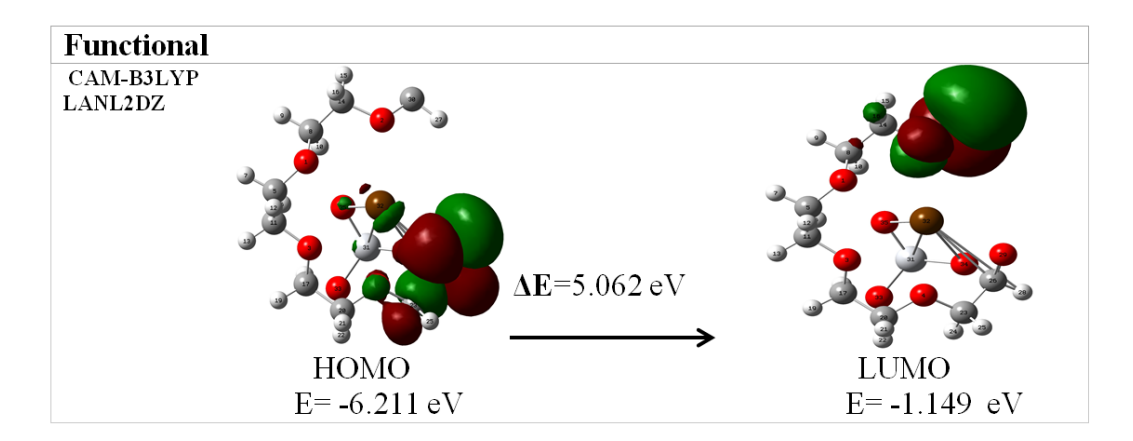
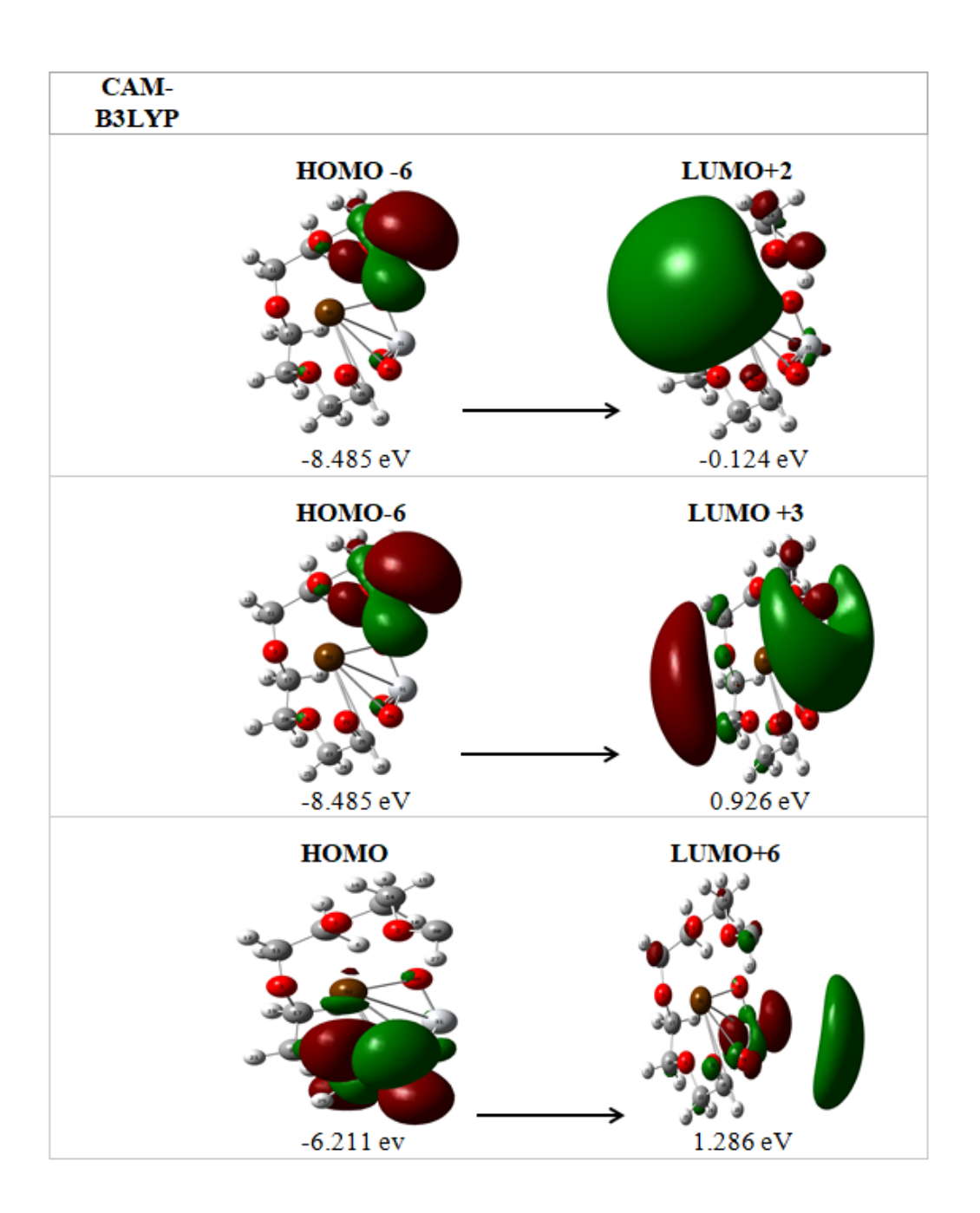


Figure 3.26: The representation of the molecular orbitals of BaTiO<sub>3</sub>/PEG optimized for each Func- tional Hybrid and their HOMO–LUMO's Energy Gap.

#### 3.8.4 UV-vis spectroscopy

The calculated electronic transition energies and the corresponding oscillator strengths (f) of the singlet excited states for compound **BaTiO3/PEG** with both CAM-B3LYP functional are reported in **Table 3.15** and the simulated spectra are depicted in **Figure 3.27**.

The absorption properties found for this compound were very similar with no significant differences in the electronic transitions. The observed absorption spectra of BaTiO3/PEG exhibit an intense absorption band in the UV region. It can be seen that the exhibits three bands of maximum absorption between 190 and 350 nm the spectra look the same. The UV spectrum shows four bands located at 330, 205.51 and 171 nm.



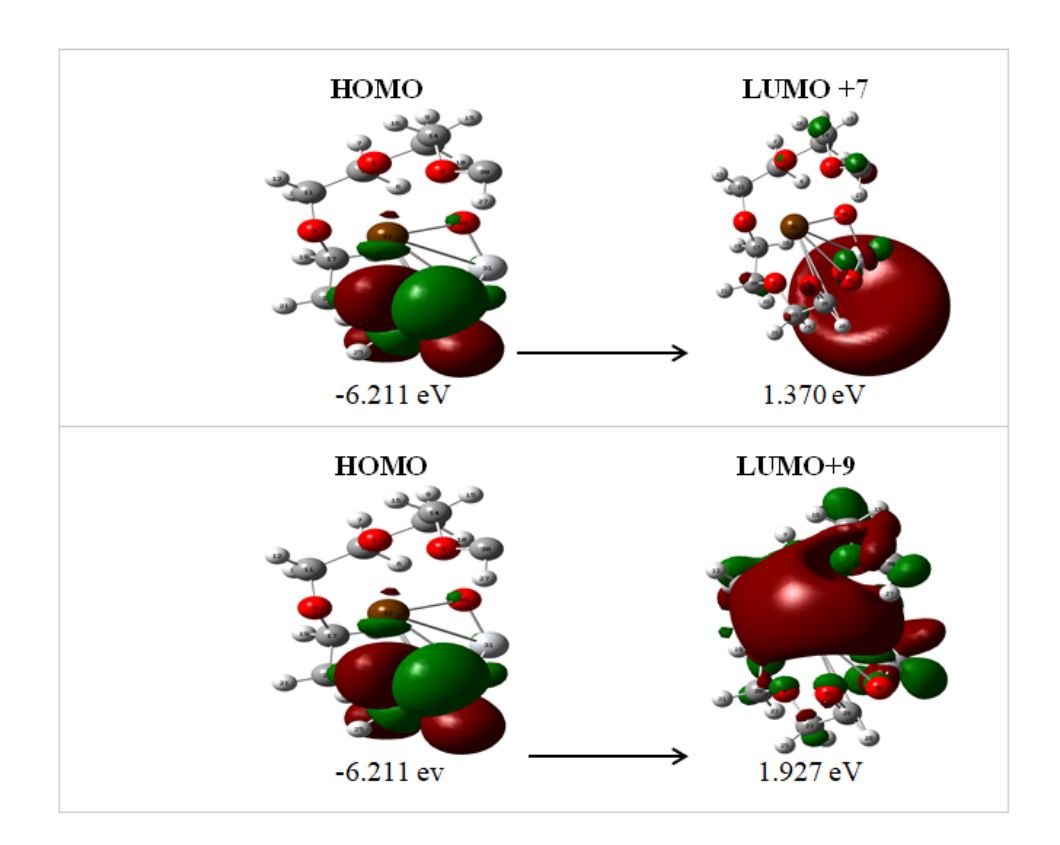


Figure 3.27: Molecular orbitals of  $BaTiO_3/PEG$  using CAM-B3LYP.

Table 3.15: : Absorption characteristics of [BaTiO<sub>3</sub>]/PEG

Functional	E <sub>exc</sub> (eV)	$\lambda_{\rm cal}$ (nm)	F	Transitional nature
CAM-B3LYP	6.033	205.51	0.0097	$56\%$ HOMO-6 $\rightarrow$ LUMO+2 $20\%$ HOMO-6 $\rightarrow$ LUMO+3 $11\%$ HOMO $\rightarrow$ LUMO+6 $16\%$ HOMO $\rightarrow$ LUMO+7 $13\%$ HOMO $\rightarrow$ LUMO+9

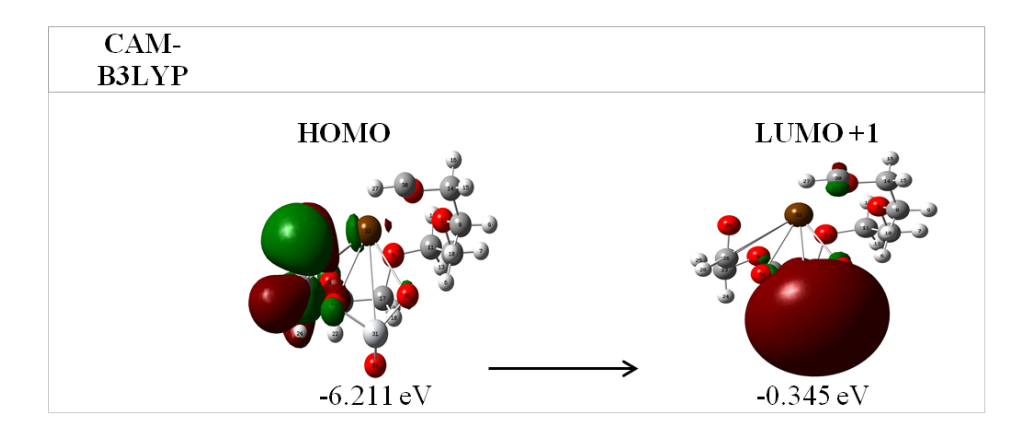
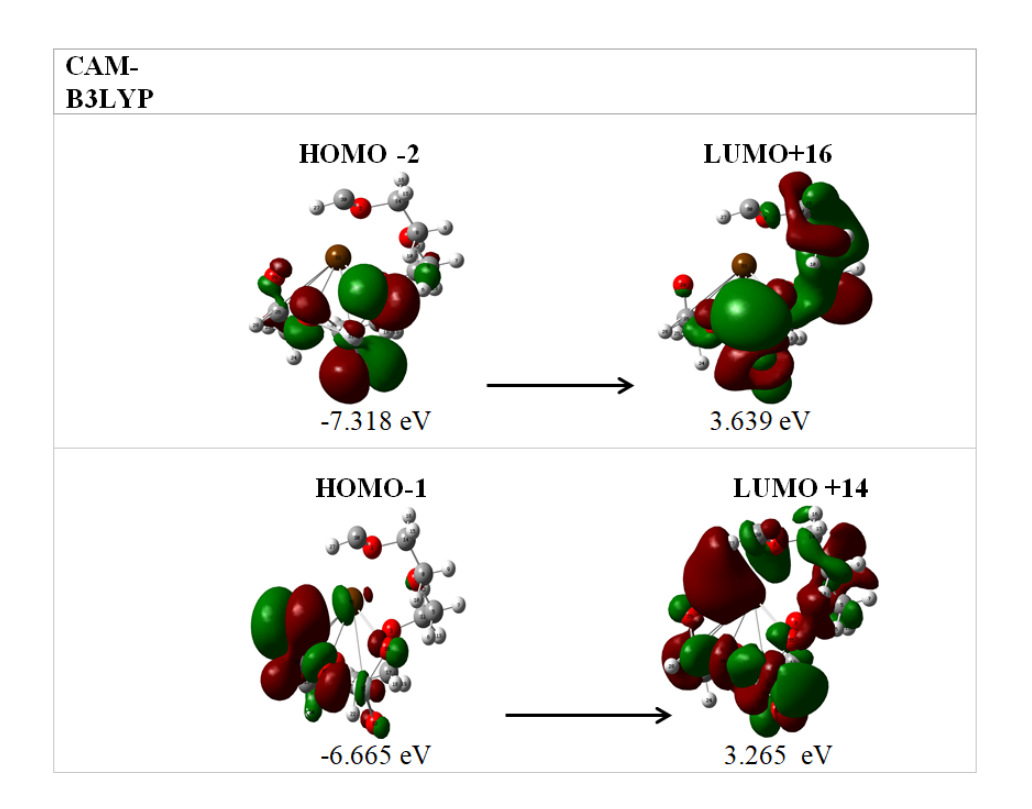


Figure 3.28: Molecular orbitals of BaTiO<sub>3</sub>/PEG using CAM-B3LYP.

Table 3.16: Absorption characteristics of the BaTiO<sub>3</sub>/PEG

Functional	$E_{\mathbf{exc}}$ (eV)	$\lambda_{\rm cal}$ (nm)	F	Transitional nature
CAM-B3LYP	3.7544	330	0.0059	60% HOMO → LUMO+1



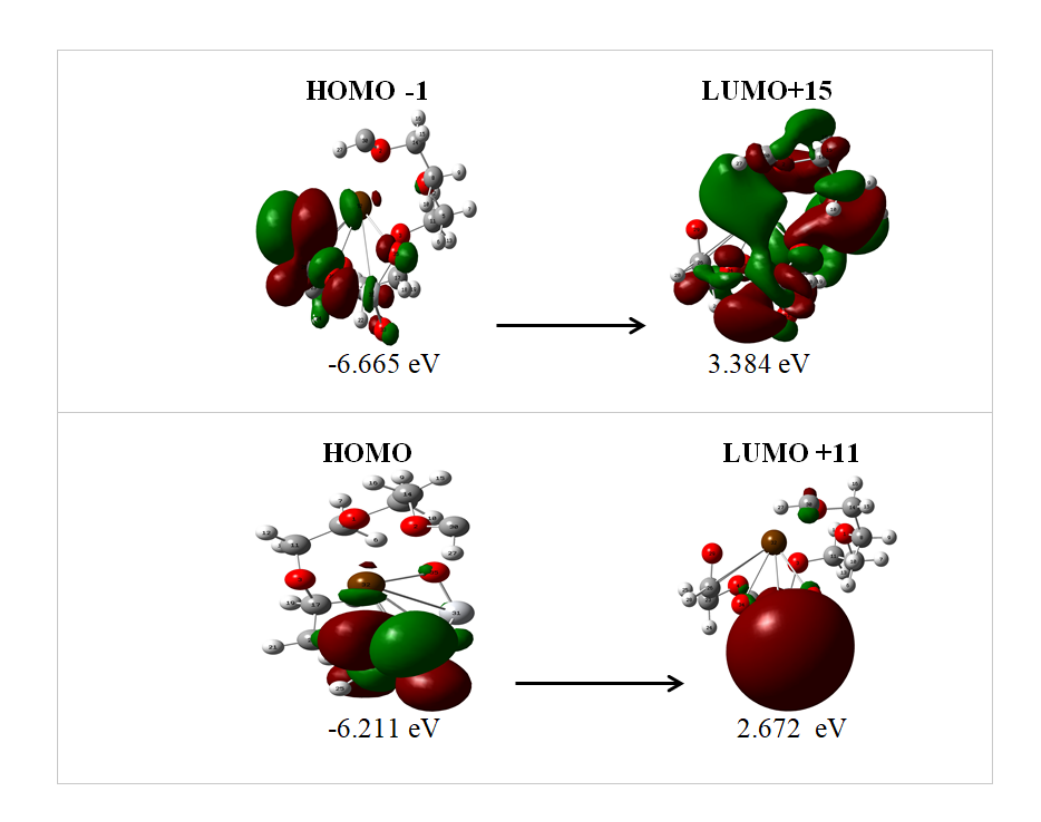


Figure 3.29: Molecular orbitals of BaTiO<sub>3</sub>/PEG using CAM-B3LYP.

Table 3.17: : CAM-B3LYP results for BaTiO $_3$ /PEG. E is the transition energy (in eV)  $\lambda_{cal}$  wavelength in (nm) and f is the oscillator strength of the excited stat

Functional	E <sub>exc</sub> (eV)	$\lambda_{\rm cal}$ (nm)	F	Transitional nature
CAM-B3LYP	7.2129	171.89	0.0251	12% HOMO-2 → LUMO+16 22% HOMO-1 → LUMO+14 11% HOMO-1 → LUMO+15 27% HOMO → LUMO11

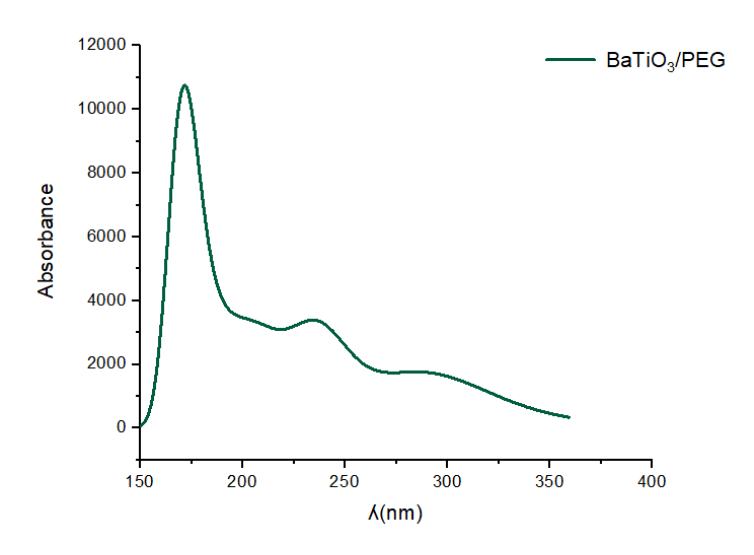


Figure 3.30: The UV-visible spectrum of BaTiO<sub>3</sub>/PEG.

#### 3.8.5 IR Vibration Frequencies:

Were performed at the same theoretical level to compare between the calculated IR spectrum of the  $BaTiO_3/PEG$  and the experimental one. The absence of imaginary frequencies in the calculated vibrational modes indicates that the obtained optimized geometry corresponds to a minimum on the potential energy surface.

The vibration at a frequency of 211 cm<sup>-1</sup>, associated with a Ba-O-C bond, is an indication of the vibration of the bond between the barium atom (Ba) and an oxycarbon group (O-C). This frequency indicates a particular vibrational mode, probably a stretching or bending vibration, characteristic of the Ba-O-C bond. The presence of the Ba-O-C vibration in the IR spectra indicates that the nanocomposite is well formed.

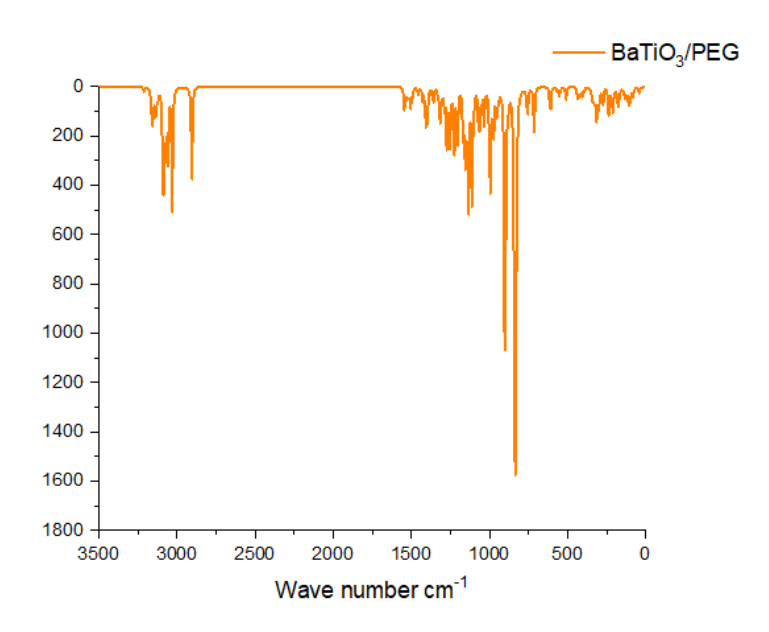


Figure 3.31: Simulated IR spectra of BaTiO<sub>3</sub>/PEG

Table 3.18: Vibrational frequencies (in  $\rm cm^{-1}$ ) in different functional and experimental values of  $\rm BaTiO_3/PEG$ .

Bond	Calculated peak (cm <sup>-1</sup> )	BaTiO <sub>3</sub> /PEG
Ti-O	833.58	3027.09
Ti–O	900.52	959.81
С-О-Н	1135.02	1100
С–Н	2905.65	2880
С–Н	3030.90	3027.09
Ва-О-С	211.93	[29]

## General conclusion

In recent years, study on polymer/ceramic composites has received much attention from academic researchers and industry because polymers are flexible, inexpensive and easily processed. Barium titanate (BaTiO $_3$ ), a perovskite-type electro-ceramic material, has interesting properties; a high dielectric constant, along with ferro-, piezo-, and pyro-electric properties. BaTiO $_3$  is widely applied in the manufacture of multilayer ceramic capacitors (MLCC), infrared detectors, thermistors, transducers, electro-optic devices and sensors .

In the current study, we have calculated the electronic properties such as energy band structure and spectroscopy properties of the  $BaTiO_3$  perovskite material and  $BaTiO_3/PEG$  nanocomposite.

The DFT and TDDFT methods using the basis set Lanl2DZ at the level of CAM-B3LYP theory can has been demonstrated to provide good results for the structure and absorption properties of the  $BaTiO_3$  and  $BaTiO_3/PEG$  compounds. All theoretical results were compared with the experiment and found to be in good agreement.

This theoretical study of the absorption properties of a BaTiO<sub>3</sub>/PEG, allowed us to extract some structure–property relationships of great significance for both spectral tuning of novel nanocomposite in the UV-Vis spectral domain.

Calculated  $\lambda_{max}$  (nm) shows an apparent change with matriau containing PEG. The present paper can provide the experimentalists with data to develop a working device using this system.

In our analysis of vibrational modes, we focused on the Ba-related vibrational modes. Ex-

periments and simulations revealed that the vibrational modes of the Ba - O-C stretching, with a wavenumber of approximately  $211~(cm^{-1})$ , corresponded to the formation of bonds between barium (Ba) and oxygen (O) on the nanocomposite.

**Part III** 

Annex 1

#### General Presentation of the Software Used

Numerical simulation in the field of molecular chemistry, as well as in related fields such as molecular biology and materials science, is a rapidly growing area of scientific computing. In fact, the development of theoretical chemistry is closely linked to advances in computing technologies. However, the computational aspect of the problem mainly concerns the software used in theoretical chemistry, both in quantum chemistry and in modeling.[59]

#### **Gaussian Software**

Gaussian is a quantum chemistry software originally developed by John Pople and first released in 1970. The software is named after its use of Gaussian orbitals, which accelerate calculations compared to software that uses Slater-type orbitals. Gaussian is used to compute the molecular conformation of molecules, including bond lengths and bond angles between atoms.

Available for most operating systems (Windows, Macintosh, Linux, etc.), Gaussian is based on the fundamental laws of quantum mechanics. It is widely considered one of the best computational chemistry programs. Gaussian enables the prediction of energies, structures, and vibrational frequencies of molecular systems, as well as many other properties. [4] It can be used to study chemical systems and reactions under a wide range of conditions, including both stable species and compounds that are difficult or impossible to observe experimentally, such as transition states.



Figure 3.32: Gaussian.

#### **GaussView Software**

GaussView is the most advanced and powerful graphical interface available for *Gaussian*. With GaussView, you can import or build the molecular structures you are interested in, set up, launch, monitor, and control Gaussian calculations, and retrieve and display results—all without ever leaving the application.

GaussView 6.0 includes many new features designed to make working with large systems of chemical interest practical and simple. It also provides full support for all the new modeling methods and functions of *Gaussian 09*.[56]



Figure 3.33: GaussView.

### **Origin Software**

Origin is a scientific data processing and analysis software for the Microsoft Windows environment, developed by OriginLab. It allows the creation of 2D and 3D graphs and includes peak analysis functions.

It can also import files in various formats such as Excel, ASCII, Mathematica, or SigmaPlot, and export graphs in formats like JPEG, GIF, and TIFE.[11]

It can also be used to perform data analysis and generate graphics in a very simple and user-friendly environment. This application was developed for engineers and scientists. All the graphs created in this work were made using version 09 of the Origin software (*OriginPro 2018*).

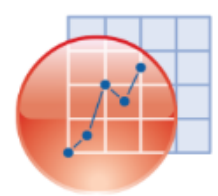


Figure 3.34: OriginPro.

## **Mercury Software**

Mercury is a free software developed by the Cambridge Crystallographic Data Centre (CCDC), originally designed as a tool for visualizing crystal structures. Mercury assists in three-dimensional visualization of crystal structures and helps with the drawing and analysis of crystal packing and intermolecular interactions.

Mercury can read file types such as .cif, .mol, .mol2, .pdb, .res, .sd, and .xyz. It also has its own file format with the file extension .mryx. [33]



Figure 3.35: Mercury.

#### ChemDraw Ultra Software

ChemDraw Ultra is a software developed in 2003 by CambridgeSoft, Cambridge. This software allows users to create three-dimensional models, visualize, analyze, and determine the properties of molecules.

It is a comprehensive program that offers users an exceptional modeling tool with an intuitive and easy-to-use interface.

To draw molecules, the Chem3D Ultra software offers the ability to construct molecules starting from ChemDraw, which is a specialized tool for drawing molecules.

All the diagrams presented in this work were created using version CHEMDRAW8.3 of the ChemDraw Ultra software.[41] [26]



Figure 3.36: ChemDraw.

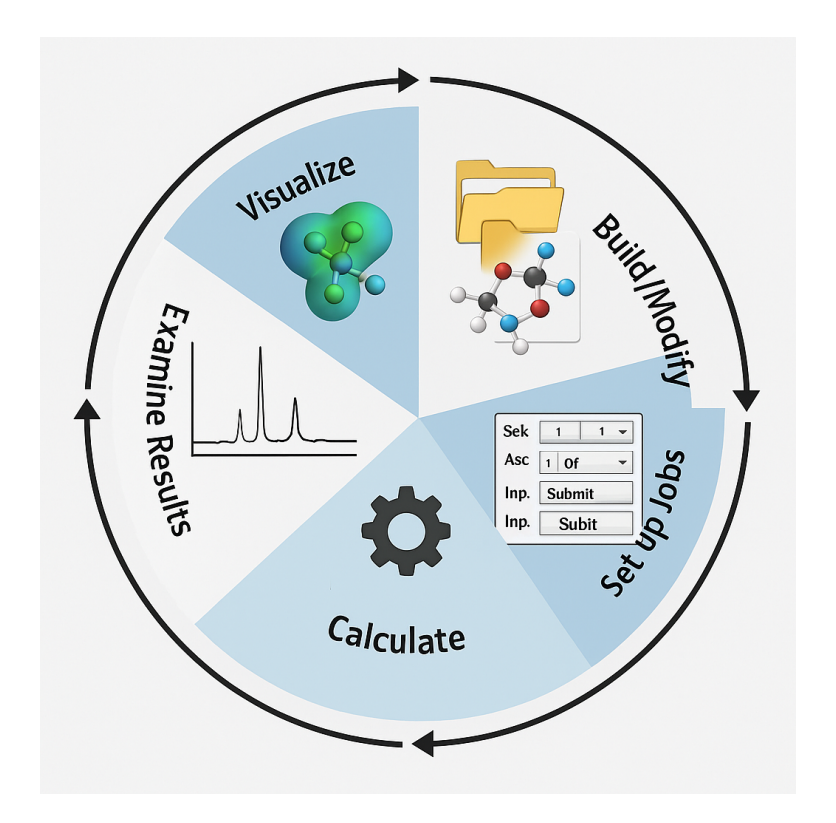


Figure 3.37: Cycle of the study of a molecule by molecular modeling..

## **Geometry Optimization**

Geometry optimization is a technique used by all computer scientists. It is a method that takes rough geometric approximations and makes them as accurate as possible. It involves a series of iterations performed on the molecule until the energy of the molecule reaches a minimum, corresponding to the stable conformations of the molecule. To begin the process, an initial geometry must be determined, followed by a series of calculations. There are three types of calculations that can be performed (molecular mechanics, semi-empirical, ab initio). Each of these calculations aims to optimize the geometry, and depending on the method used, it will

determine how accurate this optimization will be. These calculations provide not only a new geometry but also a new energy for the molecule. This process is repeated until the molecular energy reaches its minimum.

[3]

# **Bibliography**

- [1] Ahmed I Abdelamir, Ehssan Al-Bermany, and Fouad Sh Hashim. Enhance the optical properties of the synthesis peg/graphene-based nanocomposite films using go nanosheets. In *Journal of Physics: Conference Series*, volume 1294, page 022029. IOP Publishing, 2019.
- [2] Mahmoud Al-Gharram and Tariq AlZoubi. Linear and nonlinear optical properties of hybrid polyaniline/cofe2o4 nanocomposites: electrochemical synthesis, characterization, and analysis. *Ceramics International*, 50(18):32841–32852, 2024.
- [3] Salma Annane and Asma Abdelli. *Préparation et caractérisation de nouvelles formes galéniques à base d'acide niflumique et la?-cyclodextrine. Etude in-vitro et in-vivo.* PhD thesis, université ibn khaldoun-tiaret, 2020.
- [4] Hayat Ayache. *propriétés structurales et electroniques des complexes organométalliques: Etude DFT.* PhD thesis, Universite Mouloud MAMMERI Tizi-Ouzou, 2018.
- [5] Aaeid Ayoub. Études ab initio et dynamique moléculaire des propriétés structurales et thermodynamiques de la calcite et la witherite sous hautes pressions. PhD thesis, Lille 1, 2010.
- [6] Axel D Becke. Density-functional thermochemistry. iv. a new dynamical correlation functional and implications for exact-exchange mixing. *The Journal of chemical physics*, 104(3): 1040–1046, 1996.
- [7] MRA Bhuiyan, MM Alam, MA Momin, MJ Uddin, and M Islam. Synthesis and characterization of barium titanate (batio3) nanoparticle. *Int. J. Mater. Mech. Eng*, 1:21–24, 2012.
- [8] Dorsaf Bouazzi, Imen Chérif, Afef Mehri, Houcine Touati, Maria Teresa Caccamo, Salvatore Magazù, Sahbi Ayachi, Jean-Marc Clacens, and Bechir Badraoui. A joint experimental and

- theoretical study on structural, vibrational and morphological properties of newly synthesized nanocomposites involving hydroxyapatite-alt-polyethylene glycol (hap/peg). *Journal of Molecular Liquids*, 390:123192, 2023.
- [9] Praveen Chappa, Arthanareeswari Maruthapillai, Rajasekhar Voguri, Archan Dey, Subhas Ghosal, and Mohamed Amjad Basha. Drug–polymer co-crystals of dapsone and polyethylene glycol: an emerging subset in pharmaceutical co-crystals. *Crystal Growth & Design*, 18 (12):7590–7598, 2018.
- [10] Suman Chatterjee, Biljana D Stojanovic, and Himadri Sekhar Maiti. Effect of additives and powder preparation techniques on ptcr properties of barium titanate. *Materials chemistry and physics*, 78(3):702–710, 2003.
- [11] Phillip M Edwards. Origin 7.0: scientific graphing and data analysis software. *Journal of chemical information and computer sciences*, 42(5):1270–1271, 2002.
- [12] Matthias Ernzerhof and Gustavo E Scuseria. Assessment of the perdew–burke–ernzerhof exchange-correlation functional. *The Journal of chemical physics*, 110(11):5029–5036, 1999.
- [13] Burcu Ertuğ. The overview of the electrical properties of barium titanate. *American Journal of Engineering Research (AJER)*, 2(8):1–7, 2013.
- [14] E Fabiano, Lucian A Constantin, and F Della Sala. Two-dimensional scan of the performance of generalized gradient approximations with perdew–burke–ernzerhof-like enhancement factor. *Journal of Chemical Theory and Computation*, 7(11):3548–3559, 2011.
- [15] Hong-Jian Feng and Fa-Min Liu. Electronic structure of barium titanate: an abinitio dft study. *arXiv preprint arXiv:0704.2695*, 2007.
- [16] Enrico Fermi. Statistical method to determine some properties of atoms. *Rend. Accad. Naz. Lincei*, 6(602-607):5, 1927.
- [17] SELMI Oumnia Racha HABBA Nour El Houda. Les propriétés structurales et optiques des complexes macrocycliques analyse dft/tddft.

- [18] BHLB Hammer, Lars Bruno Hansen, and Jens Kehlet Nørskov. Improved adsorption energetics within density-functional theory using revised perdew-burke-ernzerhof functionals. *Physical review B*, 59(11):7413, 1999.
- [19] George G Harman. Electrical properties of bati o 3 containing samarium. *Physical Review*, 106(6):1358, 1957.
- [20] Azra Haroon, Prabhakar Rai, and Imran Uddin. Synthesis, characterization and dielectric properties of batio3 nanoparticles. *International Journal of Nanoscience*, 19(01):1950001, 2020.
- [21] J Milton Harris and Robert B Chess. Effect of pegylation on pharmaceuticals. *Nature reviews Drug discovery*, 2(3):214–221, 2003.
- [22] Fan He, Wei Ren, Guanghua Liang, Peng Shi, Xiaoqing Wu, and Xiaofeng Chen. Structure and dielectric properties of barium titanate thin films for capacitor applications. *Ceramics International*, 39:S481–S485, 2013.
- [23] Laura Jadin et al. Étude théorique des propriétés structurales et optiques de nanoparticules de cdse et de leur mécanisme de formation. 2019.
- [24] Wissal Jilani, Amel Jlali, and Hajer Guermazi. Impact of cuo nanofiller on structural, optical and dielectric properties of cuo/dgeba hybrid nanocomposites for optoelectronic devices.

  Optical and Quantum Electronics, 53:1–17, 2021.
- [25] Shabina Kappadan, Tesfakiros Woldu Gebreab, Sabu Thomas, and Nandakumar Kalarikkal. Tetragonal batio3 nanoparticles: An efficient photocatalyst for the degradation of organic pollutants. *Materials Science in semiconductor processing*, 51:42–47, 2016.
- [26] Muthukumarasamy Karthikeyan, Renu Vyas, Muthukumarasamy Karthikeyan, and Renu Vyas. Open-source tools, techniques, and data in chemoinformatics. *Practical Chemoin-formatics*, pages 1–92, 2014.
- [27] Eugene A Katz. Perovskite: name puzzle and german-russian odyssey of discovery. *Hel-vetica Chimica Acta*, 103(6):e2000061, 2020.

- [28] Eugene S Kryachko and Eduardo V Ludena. Density functional theory: Foundations reviewed. *Physics Reports*, 544(2):123–239, 2014.
- [29] Jay T Last. Infrared-absorption studies on barium titanate and related materials. *Physical Review*, 105(6):1740, 1957.
- [30] Marie L Laury, Scott E Boesch, Ian Haken, Pankaj Sinha, Ralph A Wheeler, and Angela K Wilson. Harmonic vibrational frequencies: scale factors for pure, hybrid, hybrid meta, and double-hybrid functionals in conjunction with correlation consistent basis sets. *Journal of computational chemistry*, 32(11):2339–2347, 2011.
- [31] Chengteh Lee, Weitao Yang, and Robert G Parr. Development of the colle-salvetti correlation-energy formula into a functional of the electron density. *Physical review B*, 37 (2):785, 1988.
- [32] Per-Olov Lowdin. Advances in quantum chemistry, volume 11. Academic Press, 1979.
- [33] Clare F Macrae, Ian J Bruno, James A Chisholm, Paul R Edgington, Patrick McCabe, Elna Pidcock, Lucia Rodriguez-Monge, Robin Taylor, JVD Streek, and Peter A Wood. Mercury csd 2.0–new features for the visualization and investigation of crystal structures. *Applied Crystallography*, 41(2):466–470, 2008.
- [34] Neepa T Maitra. Perspective: Fundamental aspects of time-dependent density functional theory. *The Journal of Chemical Physics*, 144(22), 2016.
- [35] Miguel AL Marques and Eberhard KU Gross. Time-dependent density functional theory. *Annu. Rev. Phys. Chem.*, 55(1):427–455, 2004.
- [36] Vikash Mishra, Archna Sagdeo, Vipin Kumar, M Kamal Warshi, Hari Mohan Rai, SK Saxena, Debesh R Roy, Vinayak Mishra, Rajesh Kumar, and PR Sagdeo. Electronic and optical properties of batio3 across tetragonal to cubic phase transition: An experimental and theoretical investigation. *Journal of Applied Physics*, 122(6), 2017.
- [37] Ágnes Nagy. Density functional. theory and application to atoms and molecules. *Physics Reports*, 298(1):1–79, 1998.

- [38] Vandana B Parmar, Dhara Raval, Sanjeev K Gupta, PN Gajjar, and AM Vora. Batio3 perovskite for optoelectronics application: A dft study. *Materials Today: Proceedings*, 2023.
- [39] A Rached, MA Wederni, K Khirouni, S Alaya, RJ Martín-Palma, and J Dhahri. Structural, optical and electrical properties of barium titanate. *Materials Chemistry and Physics*, 267: 124600, 2021.
- [40] B Sanjeeva Rao, T Venkatappa Rao, K Madhukar, C Mouli, S Kalahasti, and K Gopala Kishan Rao. Esr and ftir study of gamma irradiated poly (ethylene glycol). *Int. J. Chem. Sci*, 7: 2434–2440, 2009.
- [41] Veerasamy Ravichandran, Vishnu Kant Mourya, and Ram Kishore Agrawal. Qsar prediction of hiv–1 reverse transcriptase inhibitory activity of benzoxazinone derivatives. *Internet Electron J Mol Des*, 6:363–374, 2007.
- [42] Muhammad Rizwan, I Zeba, Muhammad Shakil, SSA Gillani, Zahid Usman, et al. Electronic, structural and optical properties of batio3 doped with lanthanum (la): Insight from dft calculation. *Optik*, 211:164611, 2020.
- [43] Osamu Saburi. Properties of semiconductive barium titanates. *Journal of the physical Society of Japan*, 14(9):1159–1174, 1959.
- [44] Sonali Saha, TP Sinha, and Abhijit Mookerjee. Electronic structure, chemical bonding, and optical properties of paraelectric batio 3. *Physical Review B*, 62(13):8828, 2000.
- [45] Simone Sanna, Christian Thierfelder, S Wippermann, Tripurari Prasad Sinha, and Wolf Gero Schmidt. Barium titanate ground-and excited-state properties from first-principles calculations. *Physical Review B—Condensed Matter and Materials Physics*, 83 (5):054112, 2011.
- [46] E Schrödinger and Collected Works. Schrödinger 1926e. Annalen der Physik, 81:109, 1926.
- [47] NN Shafeera, D Saravanakkumar, K Mohamed Rafi, A Ayeshamariam, and K Kaviyarasu. The role of batio3 nanoparticles as photocatalysts in the synthesis and characterization of novel fruit dyes is investigated. *Microscopy Research and Technique*, 88(2):523–531, 2025.

- [48] Isha Singh, Ali A El-Emam, Shilendra K Pathak, Ruchi Srivastava, Vikas K Shukla, Onkar Prasad, and Leena Sinha. Experimental and theoretical dft (b3lyp, x3lyp, cam-b3lyp and m06-2x) study on electronic structure, spectral features, hydrogen bonding and solvent effects of 4-methylthiadiazole-5-carboxylic acid. *Molecular Simulation*, 45(13):1029–1043, 2019.
- [49] MFM Taib, NH Hussin, MH Samat, OH Hassan, and MZA Yahya. Structural, electronic and optical properties of batio3 and bafeo3 from first principles lda+ u study. *Int. J. Electroactive Mater*, 4:14–17, 2016.
- [50] Llewellyn H Thomas. The calculation of atomic fields. In *Mathematical proceedings of the Cambridge philosophical society*, volume 23, pages 542–548. Cambridge University Press, 1927.
- [51] Mohammed Tihtih, Jamal Eldin F M Ibrahim, Mohamed A Basyooni, Walid Belaid, László A Gömze, and István Kocserha. Structural, optical, and electronic properties of barium titanate: experiment characterisation and first-principles study. *Materials Technology*, 37 (14):2995–3005, 2022.
- [52] M Todica, O Stan, CV Pop, Ş Răzvan, and C Niculăescu. Investigation of polyethylene glycol with embedded gold nanoparticles membranes. *Rom. J. Phys*, 65:702, 2020.
- [53] Zoltán Varga, Judith Mihály, Sz Berényi, and Attila Bóta. Structural characterization of the poly (ethylene glycol) layer of sterically stabilized liposomes by means of ftir spectroscopy. *European polymer journal*, 49(9):2415–2421, 2013.
- [54] CJ Xiao, CQ Jin, and XH Wang. Crystal structure of dense nanocrystalline batio3 ceramics. *Materials chemistry and physics*, 111(2-3):209–212, 2008.
- [55] Xin Xu and William A Goddard III. The extended perdew-burke-ernzerhof functional with improved accuracy for thermodynamic and electronic properties of molecular systems. *The Journal of chemical physics*, 121(9):4068–4082, 2004.
- [56] Alireza Yaghoubi and Ali Ramazani. Using gaussian and gaussview software for effective

- teaching of chemistry by drawing molecules. *Research in Chemistry Education*, 6(1):69–90, 2024.
- [57] Takeshi Yanai, David P Tew, and Nicholas C Handy. A new hybrid exchange–correlation functional using the coulomb-attenuating method (cam-b3lyp). *Chemical physics letters*, 393(1-3):51–57, 2004.
- [58] Xin Yang, Zhaohui Ren, Gang Xu, Chunying Chao, Shan Jiang, Shiqi Deng, Ge Shen, Xiao Wei, and Gaorong Han. Monodisperse hollow perovskite batio3 nanostructures prepared by a sol–gel–hydrothermal method. *Ceramics International*, 40(7):9663–9670, 2014.
- [59] Souad Zighmi. *Caractérisation physico-chimique des conducteurs moléculaires à base de TTF-TCNQ*. PhD thesis, 2006.

## République Algérienne Démocratique et Populaire Ministère de l'Enseignement Supérieur et de la Recherche Scientifique

Université Med Khider Biskra

الجمهورية الجزائرية التيموقراطية الشعيبة وزارة التطيم العالى و البحث العامى جامعة محمد خيضر بسكرة

> كلبة العاوم الدقيقة قسم علوم المادة شعبة الكيمياء

Faculté des Sciences Exactes Département des Sciences de la Matière Filière de Chimie

## تصريح شرفيي

## خاص بالالتزام بقواعد النزاهة العلمية لانجاز بحث

(ملحق القرار 1082 المؤرخ في 2021/12/27)

أنا الممضى أسفله،

بن براهیم میار

السيد(ة):

تخصص: كيمياء مواد

الصفة: طالب سنة ثانية ماستر كيمياء

الحامل(ة) لبطاقة التعريف الوطنية رقم: 24189018 الصادرة بتاريخ: 2019-02-12

والمكلف

علوم المادة

المسجل بكلية: علوم الطبيعية .قسم:

بانجاز أعمال بحث : مذكرة ماستر في الكيمياء

Electronic, structural and optical properties of barium titanate: DFT calculation

عنوانها:

أصرح بشرفي أنى ألترزم بمراعات المعايير العلمية والمنهجية ومعايير الأخلاقيات المهنية والنزاهة الاكاديمية المطلوبة في انجاز البحث المذكور أعلاه وفق ما ينص عليه القرار رقم 1082 المؤرخ في 2021/12/27 المحدد للقواعد المتعلقة بالوقاية من السرقة العلمية ومكافحتها

2025-05-26

إمضاء المعني بالمر